STOPPING CROSS-SECTIONS IN CARBON OF LOW-ENERGY ATOMS WITH $Z \leqslant 12$

STOPPING CROSS-SECTIONS IN CARBON OF LOW-ENERGY ATOMS WITH $Z \leq 12$

By

JOHN HARRY ORMROD, M.Sc.

A Thesis

Submitted to the Faculty of Graduate Studies

in Partial Fulfilment of the Requirements

for the Degree

Doctor of Philosophy

McMaster University

March 1963

DOCTOR OF PHILOSOPHY (1963) McMASTER UNIVERSITY
(Physics) Hamilton, Ont.

TITLE: Stopping Cross-Sections in Carbon of Low-Energy Atoms with $Z \leqslant 12$.

AUTHOR: John Harry Ormrod, B.Sc., M.Sc., (University of Manitoba)

SUPERVISOR: Professor H. E. Duckworth

NO. OF PAGES: v, 48

NO. OF FIGURES: 24

SCOPE AND CONTENTS:

This thesis is concerned with the energy loss of light atomic projectiles in thin carbon films. Chapter I gives a brief theoretical description of the processes involved and an outline of the experimental procedure. Chapter II deals with the thin carbon films used as targets in the experiments. Chapter III describes the Monte Carlo calculation used to reduce our data to information of a general form. Chapter IV contains the experimental results and Chapter V compares the results with existing data and theory.

ACKNOWLEDGEMENTS

To Dr. H. E. Duckworth, my supervisor, I offer my most sincere thanks. His kind assistance and advice were greatly appreciated.

I would also like to thank the other members of my supervisory committee, Dr. C. C. McMullen and Dr. W. W. Smeltzer. I am much indebted to Dr. W. H. Fleming for his patience in explaining computer programming techniques. I would also like to thank Dr. D. B. MacLean for the use of his micro-balance, Dr. G. W. King for the use of his evaporating unit and Dr. J. Lindhard for kindly allowing me to reproduce Figure 1 from an unpublished paper. Thanks are due to Dr. R. H. Tomlinson for suggestions on sources. Discussions with Dr. S. H. Vosko and Dr. A. Van Wijngaarden were much appreciated. Technical assistance from Mr. P. Van Rookhuyzen and the research shop is gratefully acknowledged.

This work was supported by the U. S. Air Force Office of Scientific Research and by the National Research Council of Canada.

I am indebted to the National Research Council of Canada for the scholarships awarded to me during the course of these experiments.

CONTENTS

LIST OF FIGURES

CHAPTER I

INTRODUCTION

1. Résumé.

The following describes an experimental study of the energy loss in thin carbon films of light ($Z \leqslant 12$) atoms of low energy (<150keV). In most of the cases studied, the projectiles lost energy not only to the electronic structure of the stopping medium but also through "nuclear collisions", i.e. elastic encounters with the stopping atoms themselves. The physically interesting quantities involved in the process are the electronic stopping cross-section (S_ϵ) and the nuclear (elastic) stopping cross-section (S_ν). In order to reduce our data to these quantities, a Monte Carlo calculation was performed to determine the portion of the observed stopping cross-section (S_o) which was due to nuclear collisions. This procedure yielded, by subtraction, the electronic stopping cross-section for the projectiles studied.

2. Theoretical Considerations.

The theoretical treatment of the stopping process can be divided into two related but distinct parts - the nuclear contribution from the elastic encounters with the stopping atoms and the electronic contribution from charge-exchange effects, excitation and ionization of the stopping atoms. We shall first

summarize the theory governing the nuclear stopping process, and then do the same for the electronic stopping process.

At high energies, elastic scattering is described by the well-known Rutherford formula. This formulation is only applicable when the interacting particles can be treated as point charges. In the energy interval which we are considering, the projectile is surrounded by most of its planetary electrons and, for any given nuclear collision, the penetration into the electronic cloud of the scattering centre is only partial. Hence, the description of the scattering must include the screening effects of the electrons.

Bohr (B-48) published the first detailed analysis of the nuclear stopping of low energy atomic particles in matter. Several authors have subsequently introduced refinements, the most significant contribution being that of Lindhard and Scharff (L-61).

Bohr used a Thomas-Fermi type model of the atom to describe the nuclear collisions. A screening parameter "a" (for a particular pair of atoms) is defined by the potential energy when the two particles are separated by a distance "r".

$$P(r) = \frac{Z_1 Z_2 \mathcal{E}^2}{r} e^{-\frac{r}{a}} \qquad \ldots (I\text{-}1)$$

$$a = a_0 \left(Z_1^{2/3} + Z_2^{2/3}\right)^{-\frac{1}{2}} \qquad \ldots \text{(I-2)}$$

where $\mathcal{E}$ = elementary charge

Z = atomic number

$a_0 = \frac{\hbar^2}{m\mathcal{E}}$ = Bohr radius for hydrogen

The notation used throughout the thesis is that the subscript 1 refers to the projectiles while the subscript 2 refers to the stopping atoms. Also, the subscript $\mathcal{E}$ refers to electronic collisions while the subscript ν refers to nuclear collisions.

The distance of closest approach in the unscreened case, "b", is defined by

$$b = \frac{2Z_1 Z_2 \mathcal{E}^2}{m_0 v^2} \qquad \ldots \text{(I-3)}$$

where the new symbols introduced are

m_0 = the reduced mass of the system

v = the velocity of the projectile relative to the struck atom.

Bohr then made the extremely simplifying assumption that for $b/a \gtrsim 1$, the energy loss is completely described by centre of mass isotropic scattering. He ignored electronic effects which are small compared to nuclear effects in this interval. This analysis yielded a stopping cross-section (S) which is independent of energy, in quite good agreement with

experiment. The stopping cross-section "S" is defined by

$$S = -\frac{1}{N}\frac{dE}{dx} \qquad \ldots (I\text{-}4)$$

where N = the number of stopping atoms per unit volume

$\frac{dE}{dx}$ = differential stopping power.

Bohr also analyzed the region $b/a < 1$ in which the nuclear stopping process is in the transition region between Rutherford type scattering and the isotropic scattering assumed for $b/a \gtrsim 1$. Instead of his treatment, however, we shall consider the more sophisticated approach developed by Lindhard and Scharff (L-61a). In the experiments to be described, b/a is always less than unity. For example, $b/a = 1$ for H^1 at 0.4keV and for Mg^{24} at 17keV.

In the same paper, Bohr showed that in a certain energy interval, the problem of nuclear collisions could be described classically. All of our experiments are within this interval.

The description of nuclear collisions was further refined when the differential scattering cross-section for a screened coulomb field was calculated. In doing this, Everhart et al (E-55) used the potential suggested by Bohr (Equation I-1), while Firsov (F-58) and Lindhard et al (L-61a) used the Fermi function (instead of exponential screening) to derive numerically the differential cross-section for scattering as

a function of energy.

The energy loss ΔT_ν for a single elastic collision can easily be shown to be

$$\Delta T_\nu = \frac{2 m_1 m_2}{(m_1 + m_2)^2} E (1 - \cos\Theta) \qquad \ldots (I\text{-}5)$$

where $m_1 (m_2)$ = mass of the projectile (stopping atom)

E = laboratory energy of the projectile

Θ = relative deflection angle.

The nuclear stopping cross-section can be calculated by integrating Equation I-5 over all values of Θ.

$$S_\nu = \int_0^\pi \Delta T_\nu \, d\sigma(\Theta) \qquad \ldots (I\text{-}6)$$

The results of such a procedure are shown in Figure 1 (reproduced from (L-61a) with the kind permission of Prof. J. Lindhard) where the nuclear stopping cross-section is plotted against $E^{\frac{1}{2}}$. The integration in Equation I-6 would, of course, have to be done numerically since the differential cross-section $d\sigma(\Theta)$ is not known analytically.

In turning now to the electronic stopping process, we first note that the familiar Bethe formula, $S_\epsilon \propto \frac{1}{E} \ln E$, for the electronic stopping cross-section is not valid in the energy interval which we are considering because we are well below the adiabatic limit (i.e. the projectile velocity is lower

than the orbital velocity of the electrons). Fermi and Teller (F-47) have calculated the rate of energy loss for a meson below the adiabatic limit, and their approach can be extended to heavier particles (W-49). Their argument is summarized.

The stopping medium is approximated by a degenerate electron gas. Because of the Pauli exclusion principle, only those collisions can occur which result in the final velocity of the struck electron being greater than the maximum velocity of the electrons in the gas, v_f. Hence, the number of electrons available for a collision is limited to those having initial velocities (before the collision) between v_f and $v_f - v$, where v is the projectile velocity ($v < v_f$). The result of this is that the number of electrons available for collisions is proportional to v. The average energy exchange per collision is proportional also to v. Hence,

$$\frac{dE}{dt} \propto v^2$$

and

$$\frac{dE}{dx} \propto v \qquad \ldots (I\text{-}7)$$

Lindhard and Scharff (L-61) have extended this type of analysis using the Thomas-Fermi model to determine the dependence of the electronic stopping cross-section on the atomic numbers of the interacting particles. They find

$$S_\epsilon = \xi_\epsilon 8\pi \mathcal{E}^2 a_0 Z_1 Z_2 (Z_1^{2/3} + Z_2^{2/3})^{-\frac{3}{2}} \frac{v}{v_0}$$

... (I-8)

where the new symbols introduced are

$v_0 = \mathcal{E}/\hbar^2$ = the velocity of the electron in the first Bohr orbit in hydrogen

and ξ_ϵ " is of order of 1-2, but may vary with Z_1 approximately as $\xi_\epsilon \approx Z_1^{1/6}$ ".

This equation is valid for velocities below $v_1 = v_0 Z_1^{2/3}$

From a consideration of Equation I-7 and Figure 1, we see that as a projectile slows down in this energy interval, it is subjected to a monotonically decreasing electronic stopping cross-section and a monotonically increasing nuclear stopping cross-section. The total stopping cross-section (S_t) is simply the sum of the electronic and nuclear components:

$$S_t = S_\epsilon + S_\nu$$

... (I-9)

3. Description of Apparatus.

Four types of sources were used to produce the projectile ions. An electron bombardment source was used when a convenient gas was available. Ions of the alkali metals were obtained from a single filament surface ionization source. Beryllium ions were obtained from a crucible source and magnesium ions from a Shaw source. Descriptions of these sources

can be found in (D-60).

The accelerating voltage was supplied by a Brandenburg High Voltage Generator Type MR 100/R/1. This was continuously variable from 10-80kV.

The accelerated ions were dispersed in a 10-inch 90^{o} magnetic analyzer which had a mass resolving power greater than 200. The stopping material, in the form of a carbon film, was situated at or near the principal focus of this analyzer, behind a suitable slit system. Any one of three experimental arrangements could be attached to the basic unit:

1) A 7-inch 90^{o} electrostatic analyzer, operated symmetrically, which was used to scan the energy spectrum of those ions which emerged from the film after suffering a net deflection of less than $.02^{r}$. This unit had an energy resolving power of approximately 160. This equipment, along with the magnetic analyzer, has been described by Van Wijngaarden and Duckworth (V-62).

2) A low divergence collimator (circular slits) and bellows arrangement, which was used to measure the angular distribution of all particles that emerged from the film. This is a modified version of the apparatus described in (V-62). See Figure 2-b.

3) A 7-inch 90^{o} electrostatic analyzer operated asymmetrically and mounted on a bellows arrangement, which was used to scan the energy spectrum of those

ions which emerged from the film having suffered a net deflection of $\Theta \pm .02^r$. The range of Θ was limited to $.23^r$. In this arrangement the illuminated portion of the film acted as the principal slit for the electrostatic analyzer.

In all three cases, an electron multiplier was used to detect the ions, and each event was registered on a scaler.

The geometry of both electrostatic analyzers was so arranged that the ionic charge multiplied by the voltage across the plates was one-tenth of the energy of the transmitted beam. A Beta Electric Model 2069 high voltage power supply was used as the accelerating potential to check this ratio. It was chosen instead of the regular accelerating unit because of its stability and very low ripple. The ion energies as determined by the two methods (i.e. accelerating voltage and voltage across the analyzer plates) agreed to within one part in three thousand, well within experimental error.

The voltage for the plates of the electrostatic analyzers was supplied by two Fluke Model 408A power supplies. The stated calibration accuracy of these instruments was better than 0.25%.

The significant energy differences in the experiments to be described were determined as differences in two voltage measurements. These, on

first sight, might appear to have a large possible error. However, the measurements were made in such a manner that the 0.25% applied to the difference.

The working pressure in the apparatus was approximately 3×10^{-6} torr.

4. Experimental Procedure and Analysis of the Data.

The 10-inch 90° magnetic analyzer was used to define the mass and energy of the projectiles incident on the film. Then, using one of the electrostatic analyzers, the energy profile at $\Theta = 0$ was measured. Figure 3 shows two such distributions which will henceforth be designated as ΔE curves. We define the observed stopping cross-section (S_o) at energy $\bar{E} = E_{in} - \frac{1}{2}\Delta E$ by

$$S_o = -\frac{1}{N}\frac{\Delta E}{\Delta x} \qquad \ldots (I\text{-}10)$$

where E_{in} = energy of projectile entering the film

N = 1.13×10^{23} atoms/cc (for carbon)

Δx = film thickness

ΔE = most probable energy loss.

Two different techniques were used to define the most probable energy loss. When the ΔE curve is symmetrical, as is the case for hydrogen in Figure 3, the most probable energy loss and the mean energy loss are coincident. In such cases, the most probable energy loss is taken as the difference

between the incident energy and the centre of the ΔE curve at half height. In cases where the ΔE curve is asymmetrical, as is the case for krypton in Figure 3, the experimental points were joined to form a smooth curve and the peak of this curve used to define ΔE.

An experiment with a particular ion consisted of performing measurements of this type over as wide an energy range as practicable. In the cases where doubly-charged ions could be produced, the energy range was correspondingly extended. When doubly-charged ions were used as projectiles, doubly-charged ions were also analyzed in the electrostatic analyzer. This procedure was adopted to minimize effects arising from the acquisition of electrostatic charge by the film. It was found that the film did charge up to a potential of one or two hundred volts and that, if charge states different from the incident charge state were analyzed, a considerable error was introduced. This error is quite negligible if the incident and emerging ions have the same charge.

Figure 4 shows two ΔE curves for Ne^{20} through the same carbon film. Three points should be noted:

1) The curves are both asymmetrical, consisting of a definite peak and a pronounced tail.

2) The magnitude of the tail is greater for the lower incident energy.

3) The most probable energy loss is greater for the higher incident energy.

We see that the peak behaves in the manner expected of electronic energy loss and the tail in the manner expected of nuclear energy loss.

The symmetrical profile of hydrogen (Figure 3) represents the case where the average energy loss ($\overline{\Delta E}$) is equal to the most probable energy loss. b/a is so small that the nuclear contribution is negligible (V-62) Hence, we have a direct measure of the electronic stopping cross-section and $S_o = S_\epsilon$.

For the heavier projectiles, the transmitted beam is asymmetrical. $\overline{\Delta E}$ cannot be associated with S_t because the acceptance angle of the electrostatic analyzer excludes many of the projectiles that have suffered wide-angle collisions. ΔE behaves in the general manner expected of electronic collisions but there is surely a nuclear contribution to the peak as well as to the tail, with the result that we cannot associate ΔE directly with S_ϵ. In such a case, we must sort out the nuclear contribution from the electronic. We do this with a Monte Carlo calculation.

The purpose of the Monte Carlo calculation is to determine the energy lost by the projectile to nuclear collisions in the film. This calculation is quite straight-forward, using Equation I-5 and the differential scattering cross-section. We know the total

energy loss in the film experimentally, and if the calculation gives the nuclear energy loss, the difference must be attributed to electronic effects.

The results of the Monte Carlo calculation were first compared with the angular distribution measurements, henceforth referred to as $N(\theta)$ curves. (See Figure 5). These measurements were made with the experimental arrangement shown in Figure 2-b. The slit arrangements in the apparatus are such that the experimental curves are directly proportional to $N(\theta)d\omega$. These distributions are due to nuclear collisions only, since a collision with an electron would not appreciably deflect the relatively massive projectile. It should be noted that the $N(\theta)$ curves are the results of multiple collisions.

Originally, only those results of the Monte Carlo calculation which described ions emerging from the film within the angular aperture accepted by the fixed electrostatic analyzer were compared with the experimental ΔE curves. However, the calculation itself had been arranged in such a manner that the energy distribution at all angles was calculated. In order to provide a much more convincing check on the validity of the calculation, the apparatus shown in Figure 2-a was constructed. This permitted the calculation to be compared with experiment at all angles up to .23 radians.

NUCLEAR STOPPING CROSS-SECTIONS (L61a)

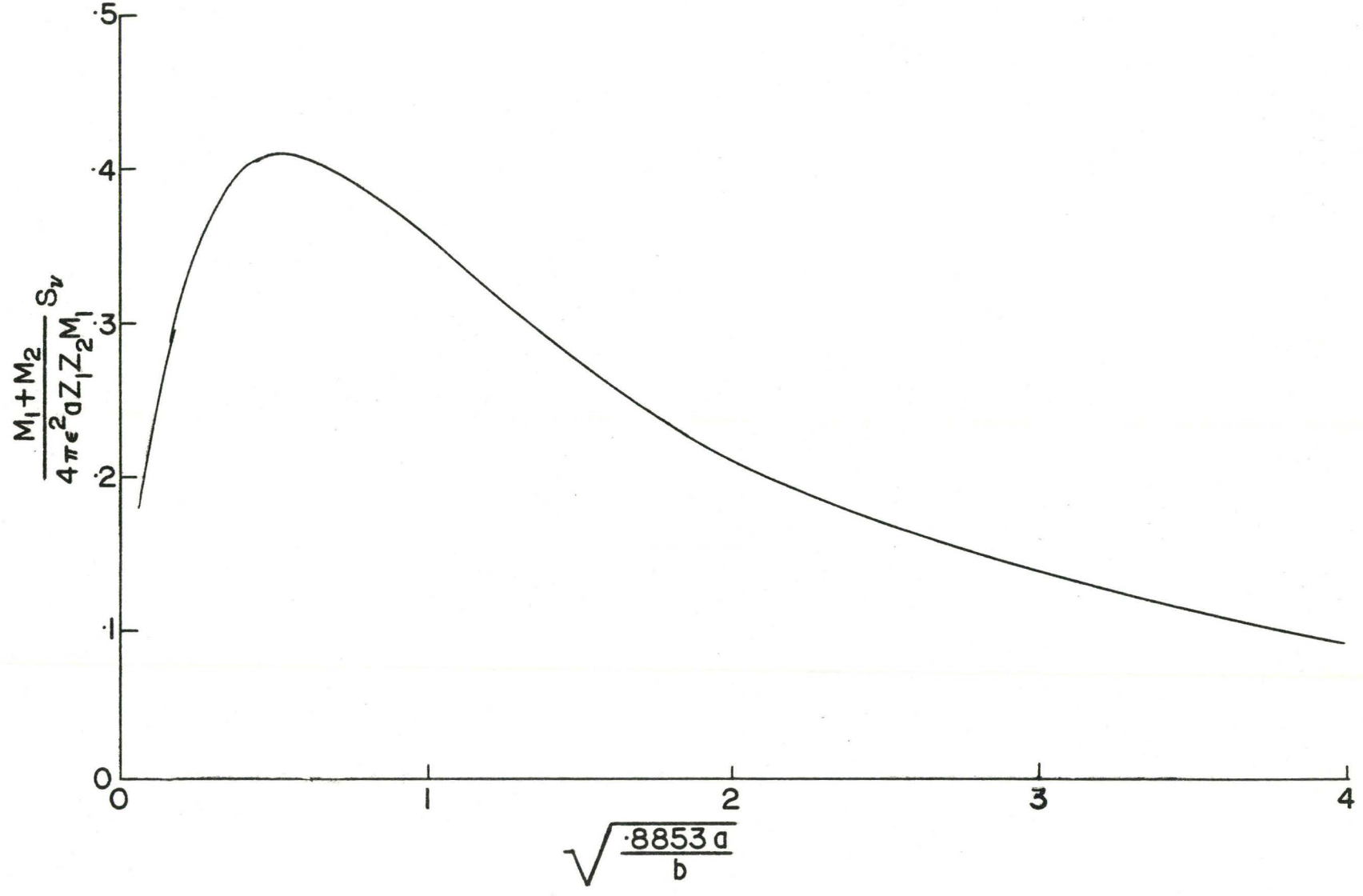

FIG. 1.

APPARATUS

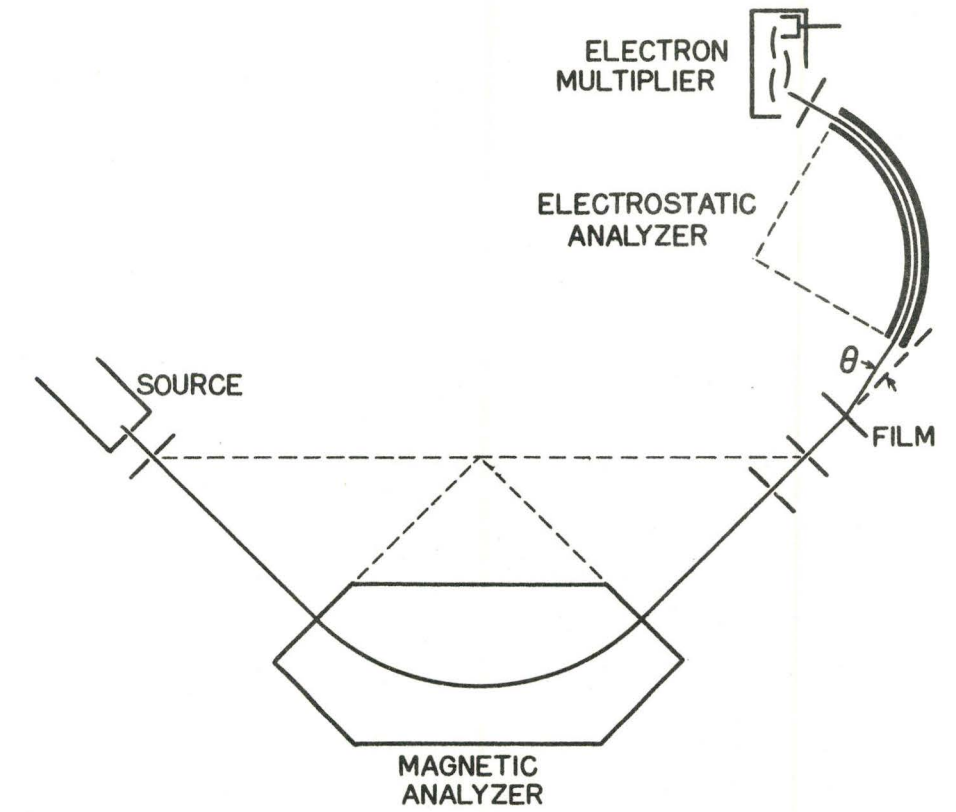

(a)

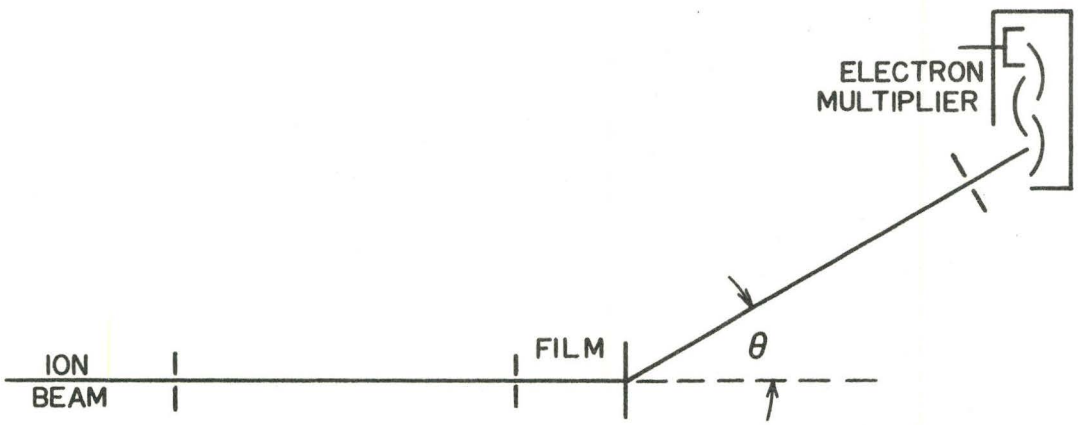

(b)

FIG. 2.

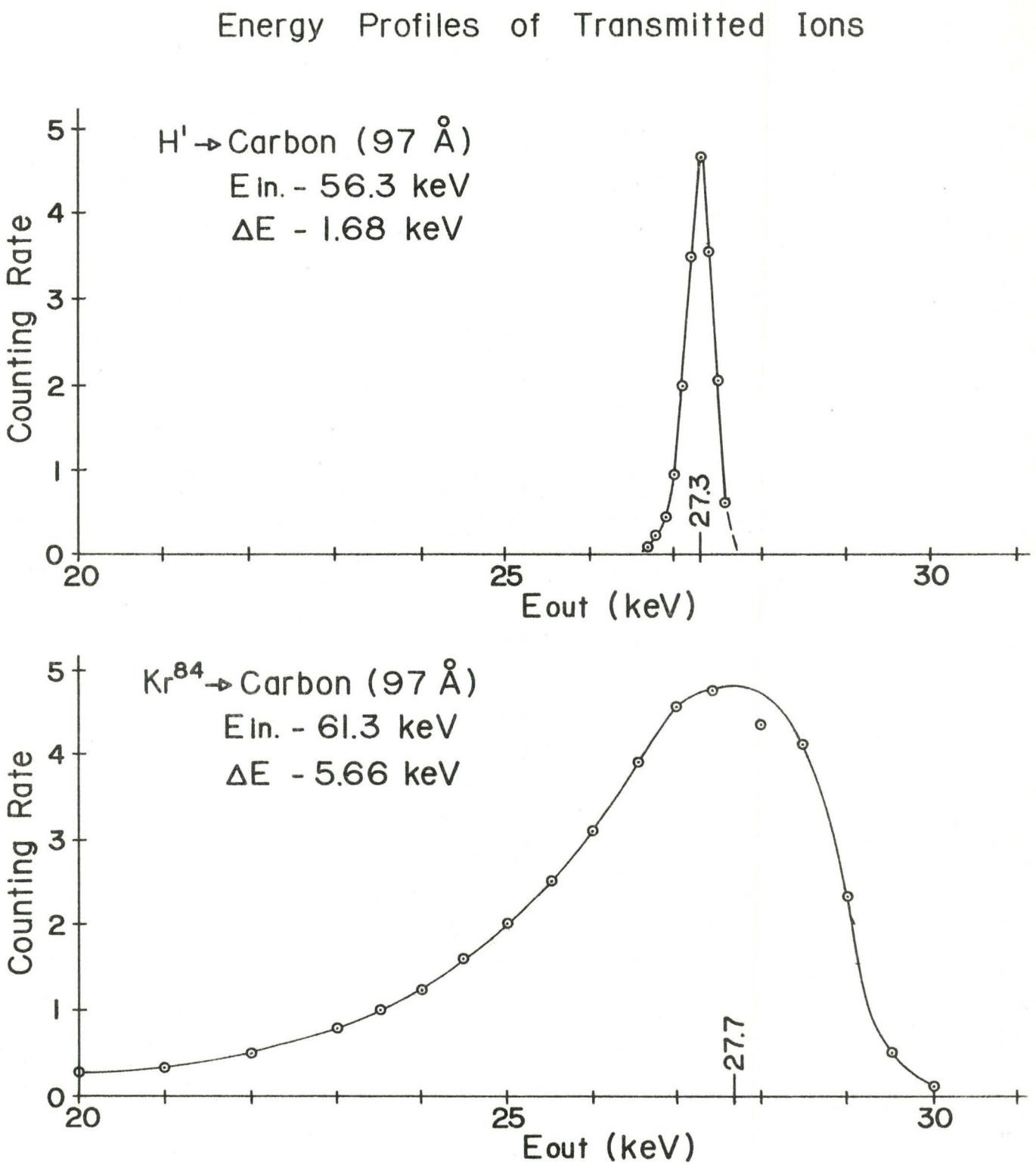
Energy Profiles of Transmitted Ions
H' → Carbon (97 Å)
E in. - 56.3 keV
ΔE - 1.68 keV
Counting Rate
Eout (keV)
27.3
Kr84 → Carbon (97 Å)
E in. - 61.3 keV
ΔE - 5.66 keV
27.7

FIG. 3.

FIG. 4.

ENERGY PROFILES $Ne^{20} \rightarrow$ CARBON (94Å)

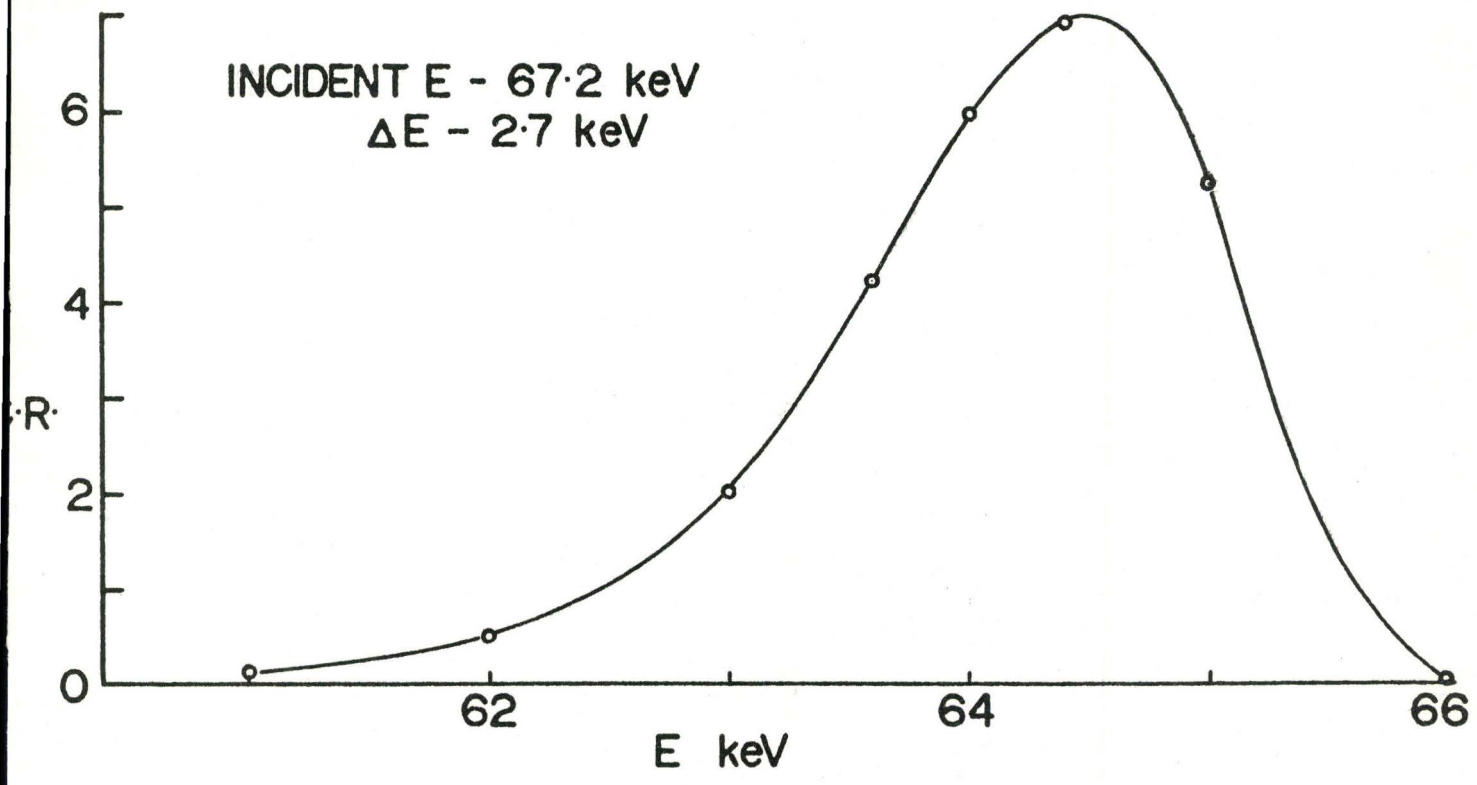

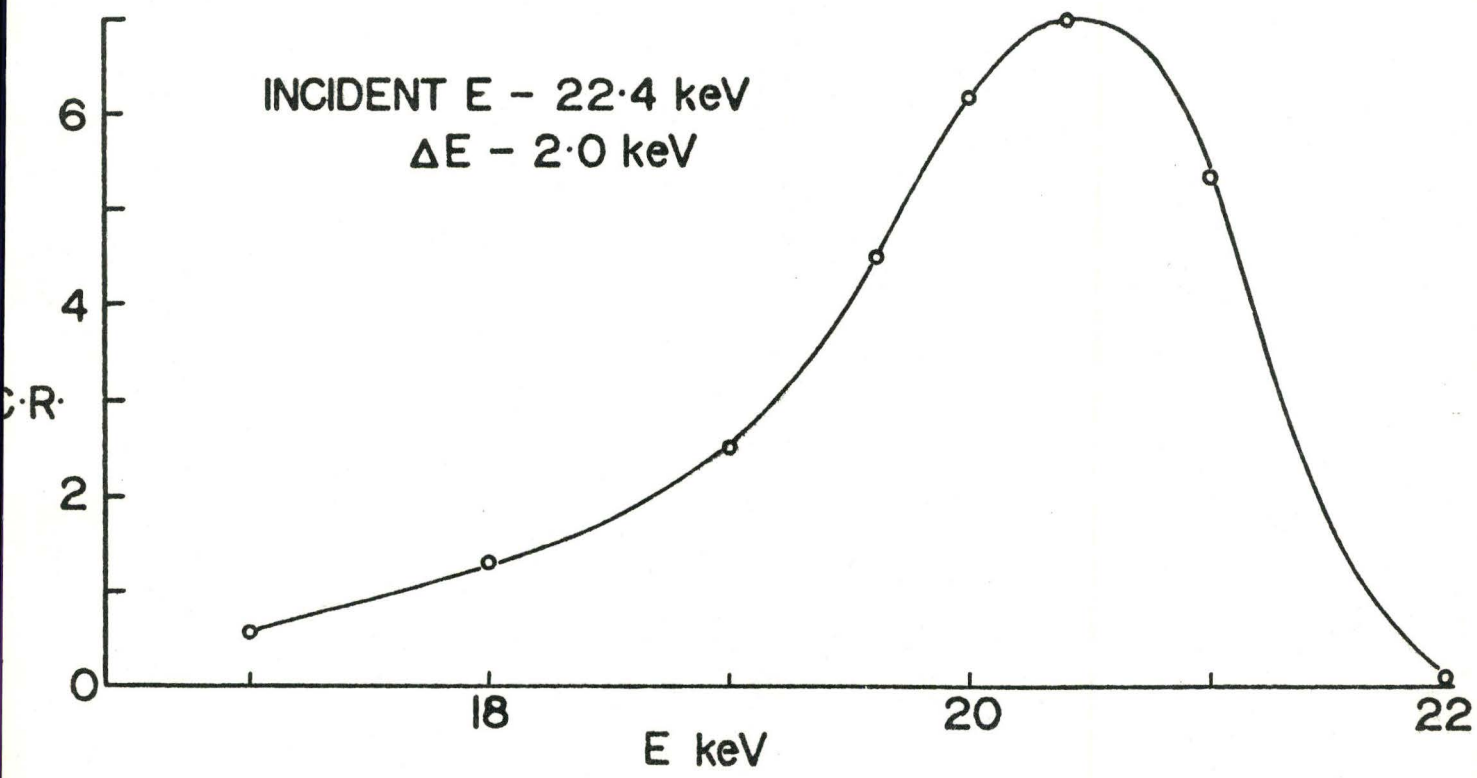

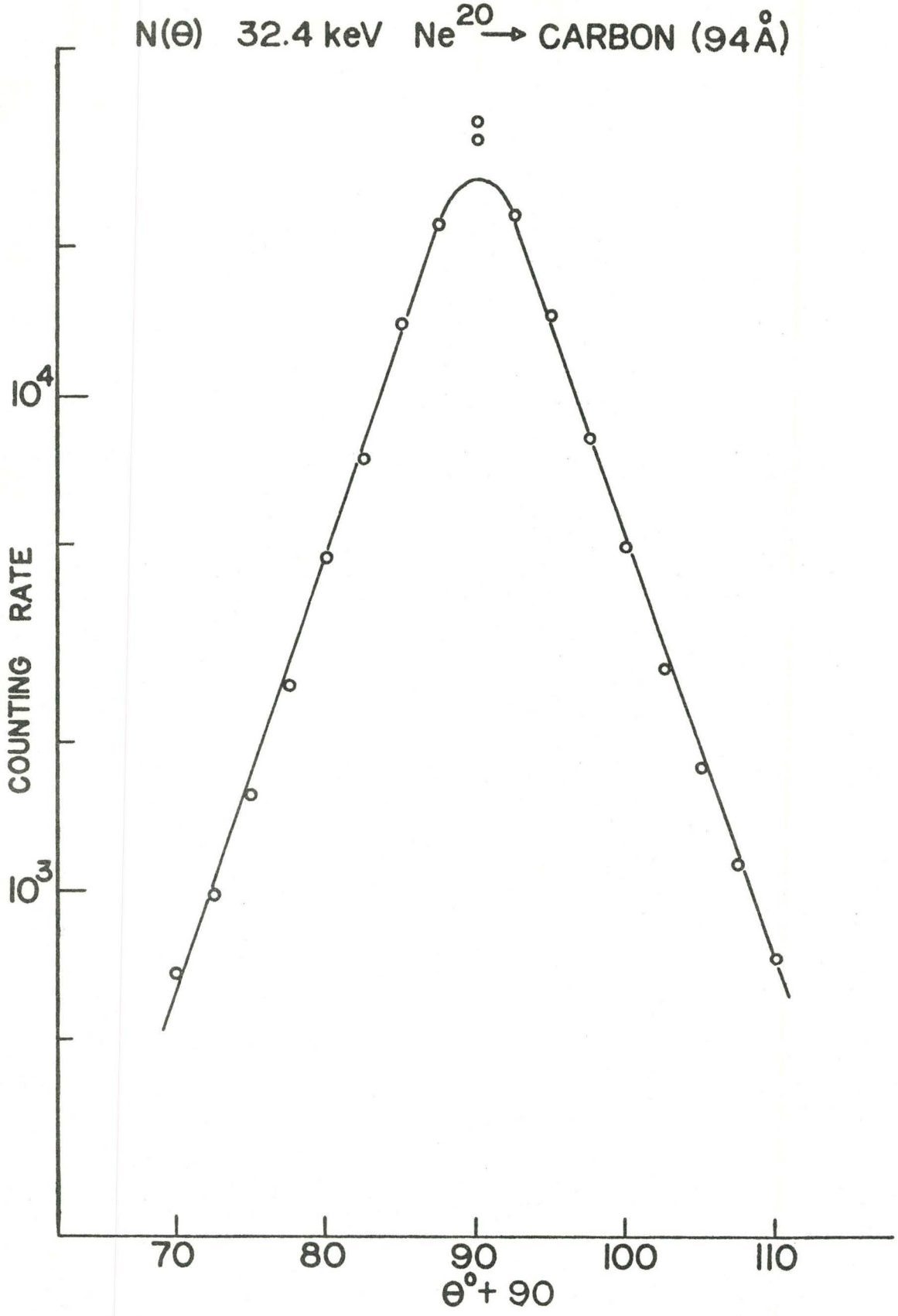
N(θ) 32.4 keV Ne20 → CARBON (94Å)
COUNTING RATE
10⁴
10³
70
80
90
100
110
θ°+ 90

FIG. 5.

CHAPTER II

THIN FILMS

1. Introduction.

The targets used in the experiments were carbon films, ranging in thickness from somewhat less than 100Å to somewhat greater than 500Å. The films were vacuum-deposited with a carbon arc onto microscope slides, using an Edwards Model 12EA coating unit. The helium-flush technique (S-61) was used. The films were removed from the slides by immersing them in water and they were then mounted on a fine nickel mesh (1000 lines per inch, 47% transmission) supported on a brass frame.

Many carbon films were used in the course of the experiments. This was necessitated by the fact that the thickness of the films increased with time. This phenomenon was not investigated in detail, but accepted as a necessary evil. To minimize this growth, the diffusion pumps were trapped continuously and the machine was vented with dry nitrogen when shut down. A film was discarded when it increased in "thickness" by 5%.

One might ask if such thin films are representative of the bulk material. Some of the films had properties that differed from others, and a consistent and reasonable criterion had to be established to test

the acceptability of any given film.

One method attempted was to measure the resistivity of the films along their greatest dimension while they were still on the glass substrate. The resistivity of carbon is $\sim$ 3500 Ω-cm and graphite is $\sim$800 Ω-cm (H-59). The measured resistivities ranged from 10 Ω-cm to 30,000 Ω-cm. The stopping cross-sections as measured with these films, however, gave consistent results. Since the resistivity had no relation to either the thickness or the stopping characteristics of the film, this method was abandoned. The reasons for this odd behaviour remain unexplained.

The criterion finally used to determine the acceptability of any given film was the ratio of the observed stopping cross-sections for H^1 and O^{16}. Two distinct groupings of films were evident. Films of 100Å or less gave one set of consistent results, and those above 140Å gave a different set of consistent results. For ion velocities above $\frac{v_o}{2}$, the results were the same for both sets of films. This behaviour was checked with H^1, He^4, Li^7, C^{12}, N^{14}, O^{16} and Ne^{20} in the energy interval 10 to 70keV.

Again, the phenomenon was not investigated in detail. The thicker films were chosen for the experiments because it seemed likely that the thinner films, if any, would be the anomalous ones.

As a final argument, the results obtained with the thicker films agreed well with other experiments

wherever a comparison was available.

2. Thickness of Carbon Films.

The energy loss of protons passing through the carbon films was used to measure their thickness. To calibrate this method, the mass deposited on a cover glass was weighed, the film removed, and the energy loss measured. Table II-1 shows the results of the six runs made. S_o is the observed stopping cross-section at 30keV as determined from several measurements.

TABLE II - 1

Run	Weight (μg)	t_w(Å)	$S_o \times 10^{14}$ (eV-cm^2/atom)	$S_o/\bar{S}_o$
1	105	434	1.24	.968
2	98	409	1.37	1.070
3	117	494	1.28	.996
4	93	388	1.19	.931
5	127	535	1.31	1.028
6	131	557	1.28	1.003

t_w is the thickness as determined with the microbalance, (Mettler Micro Gram-atic) assuming a density of 2.25 gms/cm^3. The mean stopping cross-section, ($\bar{S}_o$) was determined by statistically weighting each run by the weight of the deposit.

From the six runs, the standard deviation of S_o was calculated to be .053. This amounts to a

probable error of 2.8%. The accuracy of the microbalance is given as $\pm 2\mu g$ which, when taken with the average weight results in an error of 1.8%. We estimate the error in determining S_0 to be 1%, since it was determined from several runs. If each of these errors is treated as a probable error, the probable error for the film thickness is

$$P.E. = \sqrt{2.8^2 + 1.8^2 + 1^2} = 3.5\%$$

3. Uniformity of Carbon Films.

The films were deposited on microscope slides supported 8cm from the arc. One cause of non-uniformities was the variation in distance from the arc, a difference of 10% from the centre of the slide to the extreme edge. (The area of film illuminated by the ion beam was 1cm x .5mm, however, so that the effect in any one film was much less than 10%). This variation could have been reduced by supporting the slides a greater distance from the arc, but this would lead to a lower rate of deposition and consequently a greater impurity content. Two other sources of non-uniformity were local irregularities of the surface of the glass substrate and statistical fluctuations in the deposition of the carbon films. This latter effect was, of course, subsequently reduced as the deposited atoms sought positions of minimum potential energy.

The uniformity of the carbon films was never

measured. However, with a few assumptions, we can get an estimate of the non-uniformities from the proton straggling curves. The experimental full width at half height (Ω_o) of these curves is due to three phenomena:

1) the electronic straggling (Ω_ϵ)

2) the instrumental resolving power ($\Omega_{R.P.}$)

3) the film non-uniformities (Ω_F)

We assume that

$$\Omega_o^2 = \Omega_{R.P.}^2 + \Omega_\epsilon^2 + \Omega_F^2 \qquad \ldots \text{(II-1)}$$

$\Omega_{R.P.} = k_1 E_{in}$, where k_1 can be measured experimentally.

To find a relationship between Ω_ϵ and experimentally observed quantities we use a very simple model of the stopping process; viz. each electronic collision results in the same energy loss. If the proton suffers N collisions in passing through the film,

$$\Delta E \propto N$$

and $$\Omega_\epsilon \propto \sqrt{N}$$

i.e. $$\Omega_\epsilon^2 = k_2 \Delta E$$

To determine k_2, thick films were used (~500Å), for which Ω_F could be assumed to be negligible. Hence we now have an expression relating Ω_F to observed quantities.

$$\Omega_o^2 = (k_1 E_{in})^2 + k_2 \Delta E + \Omega_F^2 \qquad \ldots (II\text{-}2)$$

where k_1 is a constant of the instrument and k_2 is a function of the energy. For the thinner films used in the experiments, we can now calculate the non-uniformities in a film of thickness t from

$$\frac{\Delta t}{t} = \frac{\Omega_F}{2\Delta E} \qquad \ldots (II\text{-}3)$$

The results of these calculations yielded a mean variation in film thickness of $\pm$ 14Å, increasing slightly for the thicker films and decreasing slightly for the thinner films. It was assumed, however, that the 14Å figure was independent of film thickness. The films with the least non-uniformities were used in the final experiments.

It was also important that the films be free of pinholes, in order to prevent the appearance of satellite peaks. The satellite peaks appeared when the voltage across the electrostatic analyzer was such that the ion beam transmitted by the pinholes struck the outside plate of the analyzer at a point in line with the final slit system. Some of the photons so produced released photo-electrons at the conversion dynode of the electron multiplier and registered as counts. Films used in the actual experiments were chosen to be free of pinholes.

CHAPTER III

MONTE CARLO CALCULATION

1. Description.

The purpose of the Monte Carlo calculation is to determine which portion of the observed energy loss as measured with the electrostatic analyzer is due to nuclear collisions. Such an analysis is necessary when the asymmetry in the energy profile of the transmitted beam becomes pronounced.

The calculation takes an incoming projectile and allows it to suffer collisions until it has a Z-co-ordinate equal to the thickness of the film; then the computer types out the polar angle, final energy and total nuclear energy loss of the particle.

At some point in the ion's trajectory, let it be travelling with polar angle θ_n and let it suffer a collision which deflects it through a relative angle Θ. Θ yields ϕ, the angle of scattering in the laboratory co-ordinate system. The resultant direction of the ion, θ_m, lies between $\theta_n + \phi$ and $\theta_n - \phi$ since the scattering event has equal probability everywhere on the cone of half angle ϕ. If α is defined as the azimuthal angle at the base of the cone of half angle ϕ, then

$$\cos\theta_m = \cos\theta_n \cos\phi + \sin\theta_n \sin\phi \cos\alpha \qquad \ldots \text{(III-1)}$$

where α has equal probability for all angles.

The distribution in Θ comes from the differential cross-section for a screened coulomb field. Everhart et al (E-55) have calculated $\sigma(\Theta)$ for different values of b/a using the exponential atomic model suggested by Bohr (B-48). Firsov (F-58) and Lindhard et al (L-61a) have calculated $\sigma(\Theta)$ from the Thomas-Fermi model of the atom. We use the results of Lindhard et al (L-61a) in our calculations.

The angular deflection Θ for each collision is determined in the following manner. The plot of the differential cross-section versus Θ is divided into sections, and the area A_i and the mean scattering angle $\overline{\Theta_i}$ calculated for each section. The probability of the collision having $\Theta = \overline{\Theta_i}$ is proportional to the area of the i^{th} section. The total area represents σ_T, the total cross-section. 1024 memory locations in the computer are used to store $\sigma(\Theta)$, the number allotted to $\overline{\Theta_i}$ corresponding to the area under the i^{th} section. For each collision a random number is generated which modifies the command to pick up Θ, each of the 1024 memory locations having equal probability of being chosen. This provides a random variation of Θ weighted to correspond to the shape of the differential cross-section curve. The differential cross-section is a function of energy as one can see from Figure 6, which shows $\sigma(\Theta)$ for Kr^{84} colliding with C^{12} (abbreviated $Kr^{84} \rightarrow C$) at 30 and 64keV. While the total cross-section has changed by

almost a factor of two, the relative cross-section (i.e. the shape of the curve) has not changed appreciably. This variation is easily accommodated by allowing the total cross-section to be a function of energy. What one stores in the computer is the relative cross-section, which is reasonably constant over the energy interval involved in any given calculation.

The term total cross-section' used in the preceding discussion differs somewhat from the accepted meaning of the expression. We use it to denote the cross-section for collisions that result in a relative deflection angle greater than Θ_{min}. In actually passing through the film, individual projectiles will, of course, experience collisions less than Θ_{min}. However, from the point of view of both the energy loss and scattering angle, it is very difficult to differentiate between a particle that has suffered one or several extremely gentle nuclear collisions and one that has suffered no collisions at all. By ignoring these gentle collisions, we derive two main advantages. Computing times are shortened because σ_T is smaller, yielding a longer mean free path; hence fewer collisions occur in passing through the film. We are not concerned with nuclear collisions that require description by the Born approximation, since in every case Θ_{min} is chosen to be well within the bounds required for the classical description of the collisions. In choosing Θ_{min}, care

must be exercised so that neither the $N(\theta)$ distribution nor the energy profile are affected.

Figure 7 is a flow diagram of the computer program. A Bendix G-15 general purpose computer was used. Approximately 20 hours of computer time were required at each energy studied.

2. Comparison with Experimental Results

Most of the calculations were performed for neon projectiles. However, we shall show in the next section that the results can be extended to neighboring ions.

The calculated results were compared with both the $N(\theta)$ measurements and the ΔE curves for different angles of emergence. We shall first consider the comparison with the $N(\theta)$ measurements and some tests that were performed to check the validity of our assumptions.

We assume that θ_{min} can be chosen to have a negligible effect on both the $N(\theta)$ distribution and the energy spectrum of the transmitted projectiles. This is plausible if one considers that as θ_{min} is decreased, the total cross-section is increased, resulting in more collisions with a smaller average scattering angle.

The whole problem is further complicated by the fact that the differential cross-section has been calculated for free scattering centres, while the carbon atoms in our experiments are bound in some sort of structure. This fact imposes an immediate lower limit on θ_{min}. What meaning can be ascribed to a collision

with impact parameter greater than half the lattice spacing? An even more severe restriction is the effect of the lattice binding. Seitz (S-56) has estimated the displacement energy (i.e. the energy required to disrupt completely the bonds holding an atom in its lattice site) to be 25eV. For collisions resulting in an energy transfer much below this limit, one might expect the differential cross-section to deviate appreciably from that for a free scattering centre.

To determine how these effects influence our results, three calculations were performed for the same experimental conditions, differing only in the value for Θ_{min} used in the differential scattering cross-section. The values chosen were $\Theta_{min} = .038^r$, $.027^r$ and $.019^r$ which correspond to minimum energy transfers of 12eV, 6eV and 3eV. The results of these calculations and the comparison experimental curve are shown in Figure 8. The experimental curve has been folded at $\Theta = 0$ and averaged to eliminate any asymmetries due to stray magnetic fields. It is drawn as the solid line. The results of the calculations, which would normally be shown as histograms, are here represented by individual points for greater clarity.

The calculated $N(\Theta)$ distribution is in each case normalized to the experimental result for best fit. Actually, they should be normalized to equal areas (i.e. the same number of ions). This method is not used because

the calculation determines $N(\theta)d\theta$ while the experiment measures $N(\theta)d\omega$. If we normalize to equal areas, the $\sin\theta$ factor ($N\theta\, d\theta \propto \sin\theta N(\theta)d\omega$) gives a disproportionate weight to those results near $\theta = 0$ and we lose the advantage of the better statistics at larger θ.

The general agreement of all three calculations with the experiment is good. The calculated points at the smallest value of θ are all low. This was found to be the case in general, apparently eliminating the possibility of a statistical fluctuation accounting for the discrepancy. We interpret the consistent difference as being due to either a weakness of the calculation or an error in the differential cross-section. In either case, the effect on the results should be small. It should also be noted that the film used in the experiment was of the anomalous variety, but this should have no effect on the nuclear component of the energy loss since the anomaly is an electronic phenomenon. Figure 9 compares the calculation and experiment at a higher energy.

Figure 10 shows the experimental and calculated ΔE curves at four values of θ. There is no comparison at $\theta = 0$ because the statistics from the calculations are poor. The calculated curves are normalized to the same areas as the experimental curves. The peak of the calculation is generally more pronounced than that of

the experiment. This is to be expected since the experiment includes two phenomena not incorporated in the calculation - electronic straggling and straggling due to film non-uniformities. The calculated ΔE distributions also display a marked granularity. We believe this is caused by the fact that $\sigma(\theta)$ is stored in the computer as a group of delta functions instead of a smooth continuous distribution. We have already interpreted the tail as a nuclear phenomenon. Since the calculation is intended to reproduce the nuclear collisions in the film, we should expect good agreement between the calculated and experimental tails, which is indeed the case. It should also be noted that as θ increases, the calculation follows the experimentally determined decrease in energy of the peak.

In the computation, we approximate the electronic energy loss by assuming it to be given by a constant multiplied by the path length. The value assigned to the constant is regarded as a first approximation to it. The only quantity of importance derived from the calculation is the nuclear energy loss, inasmuch as we determine the electronic energy loss by subtracting the nuclear component from the total energy loss. Therefore, we must adjust the position of the calculation along the energy axis for the best fit. This, in effect, amounts to adjusting the constant to its proper value.

As mentioned previously, the experimental peak

is less pronounced because of electronic straggling and straggling caused by film non-uniformities. To account best for these phenomena, the calculated and experimental curves are adjusted by eye so that a uniform spreading of the calculated peak would best repeat the experimental curve. This is done independently for each value of Θ. The final adjustment is an average of the four independent results. The average absolute difference from the mean is chosen as a measure of the error in this matching.

To determine S_ϵ from the calculation, the total nuclear energy loss ($\Sigma \Delta T_v$) corresponding to the peak of the calculation is subtracted from the total experimental energy loss to give the electronic energy loss. The errors in determining S_ϵ for the calculation shown are listed below:

1) Probable error in determining ΔE (estimated) = 3%
2) Probable error in film thickness = 3.5%
3) Probable error in matching calculation and experiment .2/3.88 = 3.1%

P.E. in S_ϵ $= \sqrt{3^2 + 3.5^2 + 3.1^2}$ = 5.6%

The Monte Carlo calculation was performed for Ne^{20} onto carbon at four different energies - 20, 35, 60 and 100keV. Above 100keV, the correction is sufficiently small that S_0 is practically identical with S_ϵ. The results of these calculations are shown

in Figure 20. We assume that in this energy interval S_ϵ can be represented by

$$S_\epsilon = kE^P \qquad \ldots \text{(III-2)}$$

At least two justifications exist for such an assumption. Theory predicts such an equation with P = 0.5. Experimental results where no correction is required display such a form, although the exponent, in general, is slightly less than 0.5.

The calculated points were fitted to such a curve by eye. This method is preferable to a least squares fit since S_ϵ must approach S_o asymptotically. The value of P is .47, in reasonable agreement with the values of the exponents found for other cases where no correction is required.

3. Extending Results to Other Ions.

Lindhard et al (L- 61a) have shown that nuclear stopping can be completely described by the parameter, b/a. (See Figure 1). At constant b/a, the nuclear stopping in carbon for atom A is related to that for atom B by

$$\frac{S_{nA}(M_A+12)}{24\pi\epsilon^2 a_A Z_A M_A} = \frac{S_{nB}(M_B+12)}{24\pi\epsilon^2 a_B Z_B M_B} \qquad \ldots \text{(III-3)}$$

where all symbols are as previously defined. This equation follows directly from the co-ordinates of

Figure 1.

We now define S_ν^* for any element as

$$S_\nu^* = S_o - S_\epsilon \qquad \ldots \text{(III-4)}$$

S_ν^* is that portion of the nuclear stopping cross-section seen by the electrostatic analyzer. We assume that at constant b/a

$$\frac{S_{\nu A}^*}{S_{\nu A}} = \frac{S_{\nu B}^*}{S_{\nu B}} \qquad \ldots \text{(III-5)}$$

This equation states that in comparing atom A with atom B the ratio of the energy loss of the forward scattered atoms is directly proportional to the average energy loss. This is plausible, since the differential cross-section in both cases is identical.

If the observed stopping cross-sections through the same film are known for any two elements, and the electronic stopping cross-section is known for one of these elements, then the electronic stopping cross-section for the second element can be determined by using Equation III-4 and

$$S_{\nu B}^* = \frac{a_B Z_B M_B (M_A + 12)}{a_A Z_A M_A (M_B + 12)} \qquad \ldots \text{(III-6)}$$

This procedure was used to extend the calculation for neon to the other nearby elements that were studied. The points calculated by this technique give electronic

cross-sections whose exponents, P, are closely similar to those found for atoms that have a negligible nuclear component. For decreasing Z, the magnitude of the correction decreases, and we apply this technique with confidence. For increasing Z, the magnitude of the correction increases quite rapidly, and an extension beyond Mg may introduce errors. For elements with higher Z, further calculations are required.

As a check on this technique, a Monte Carlo calculation was performed with Na. The calculated point agreed within experimental error with S_ϵ as determined from the extrapolation procedure. This is shown in Figure 21.

One might object to the procedure of extending the results for S^*_ν to low Z projectiles on the grounds that the Thomas-Fermi model is not applicable. However, the magnitude of the correction decreases as Z decreases, and for low Z projectiles the electronic stopping cross-sections are essentially determined in a region where no correction is required.

FIG. 6.

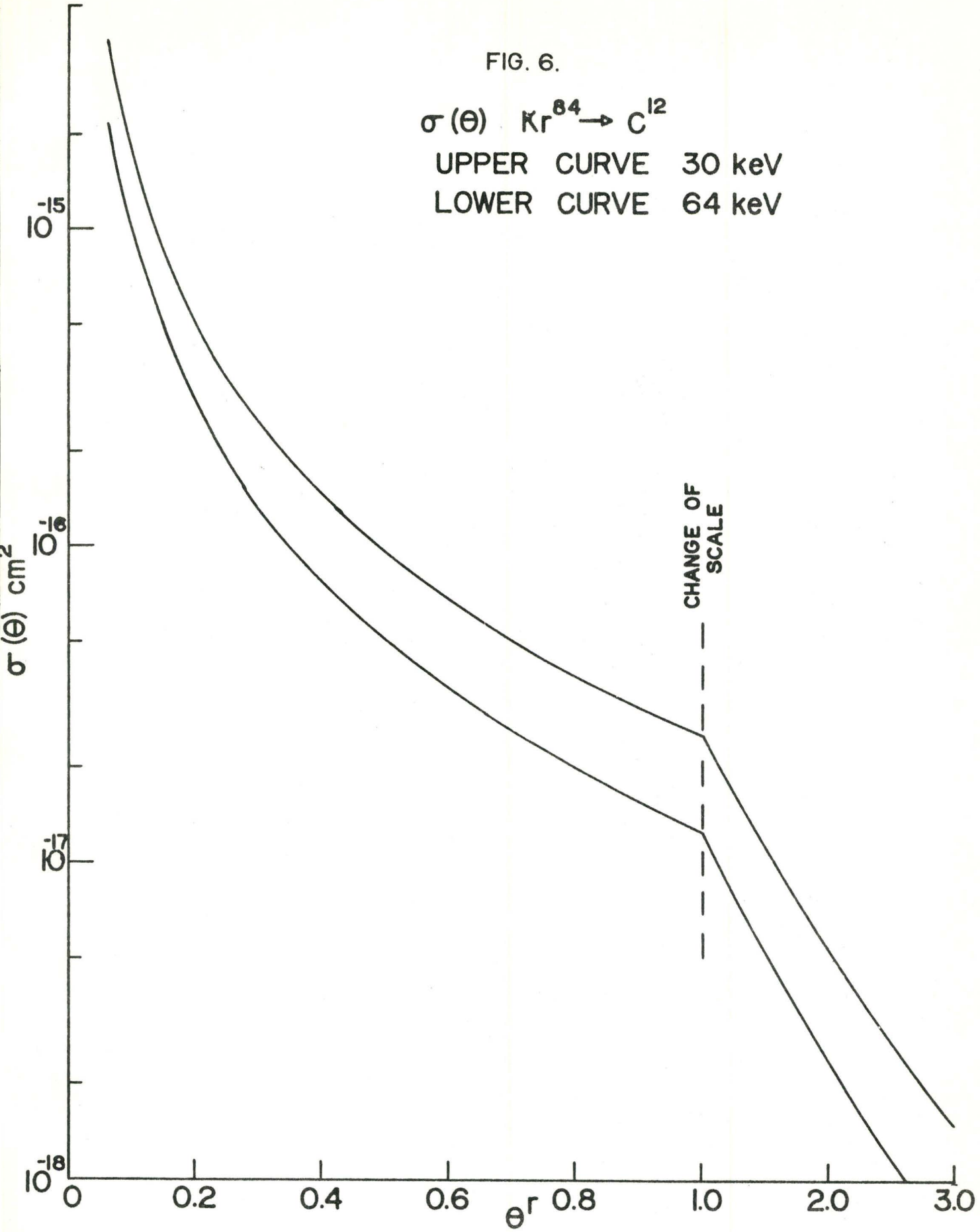
σ (θ) Kr^84 → C^12
UPPER CURVE 30 keV
LOWER CURVE 64 keV
CHANGE OF SCALE
σ (θ) cm^2
10^-15
10^-16
10^-17
10^-18
0
0.2
0.4
0.6
θr 0.8
1.0
2.0
3.0

FLOW DIAGRAM OF MONTE CARLO PROGRAM

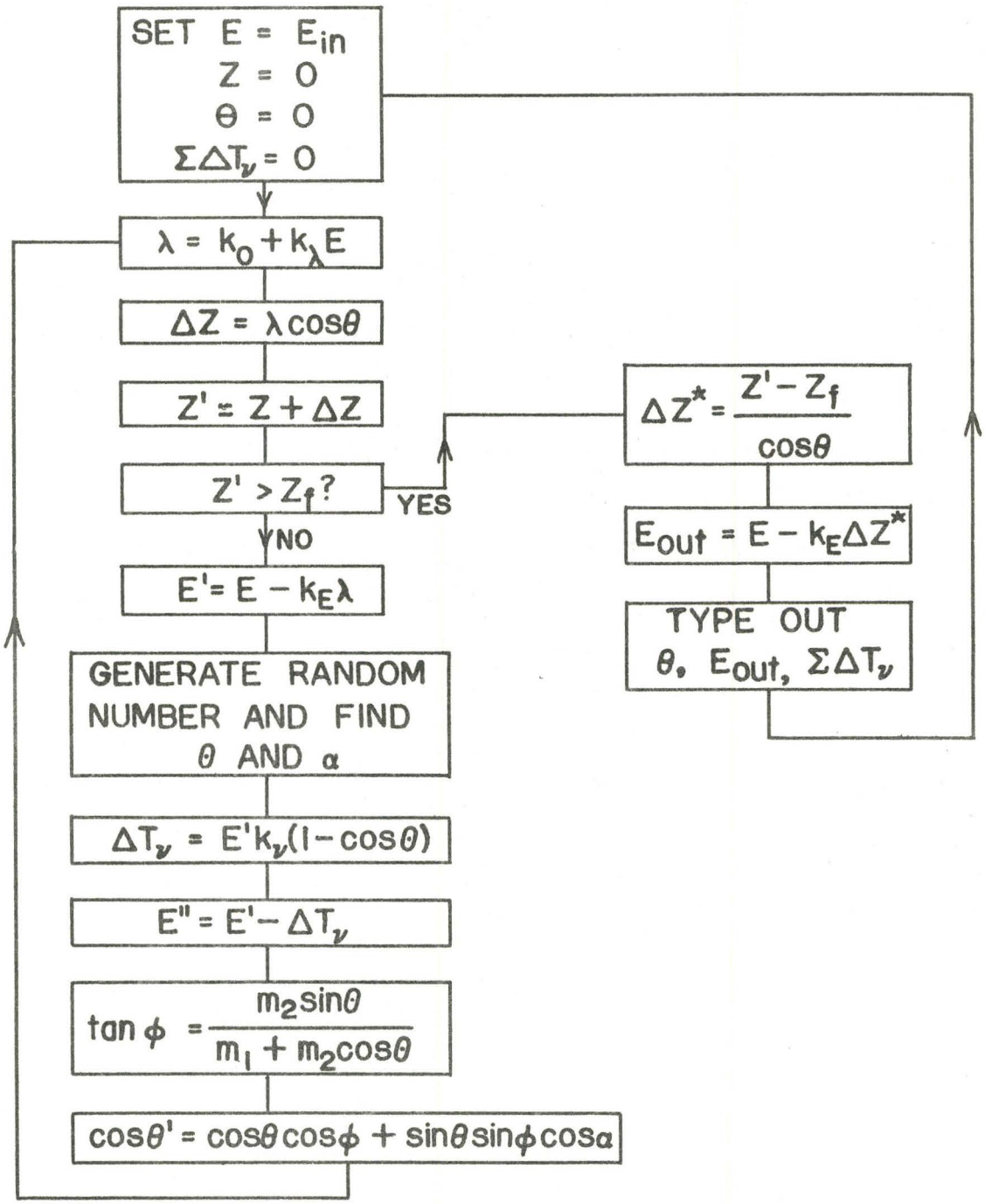

FIG. 7.

ANGULAR DISTRIBUTION OF EMERGING IONS
36 KEV $Ne^{20} \rightarrow$ CARBON (97A)

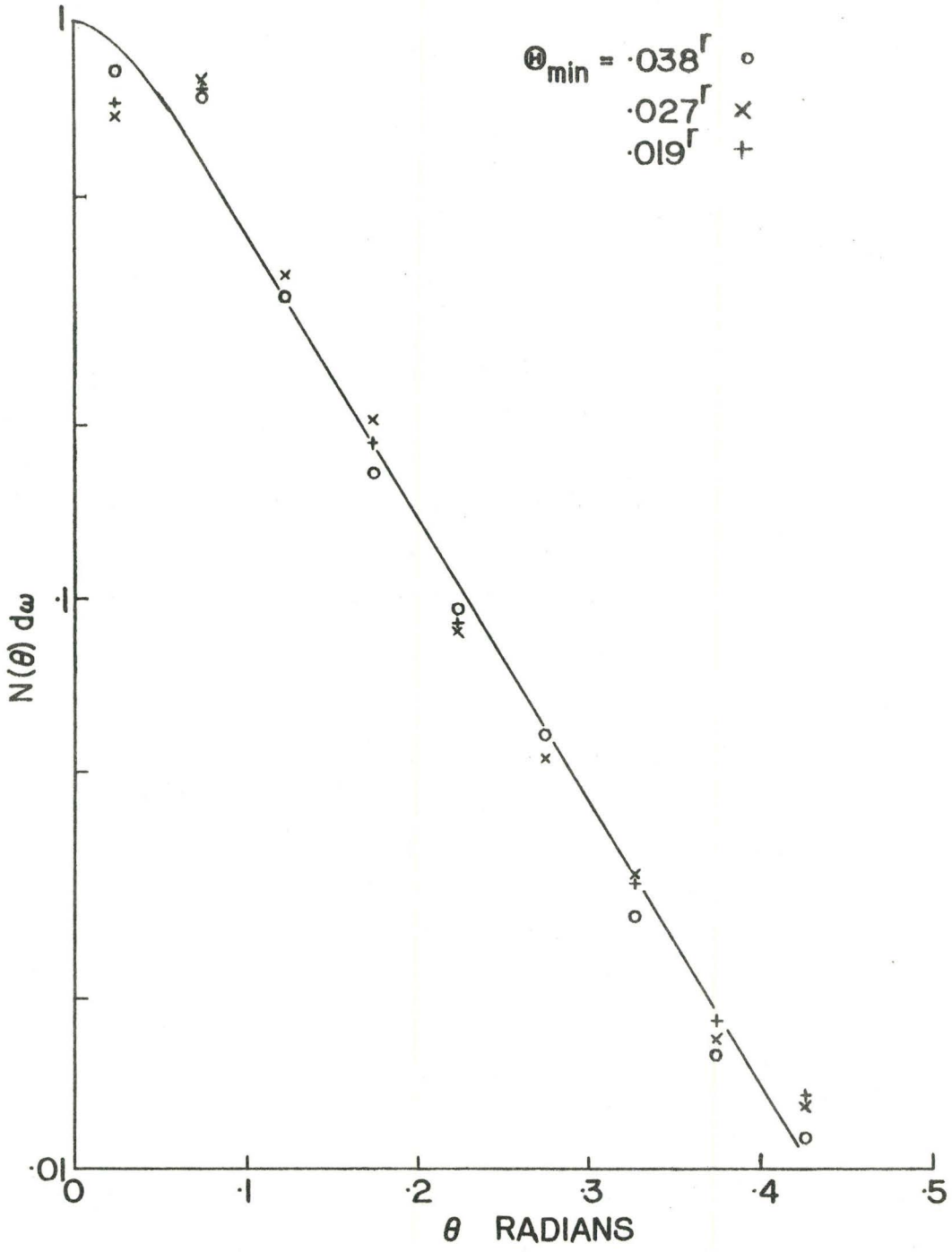

FIG. 8.

FIG. 9.

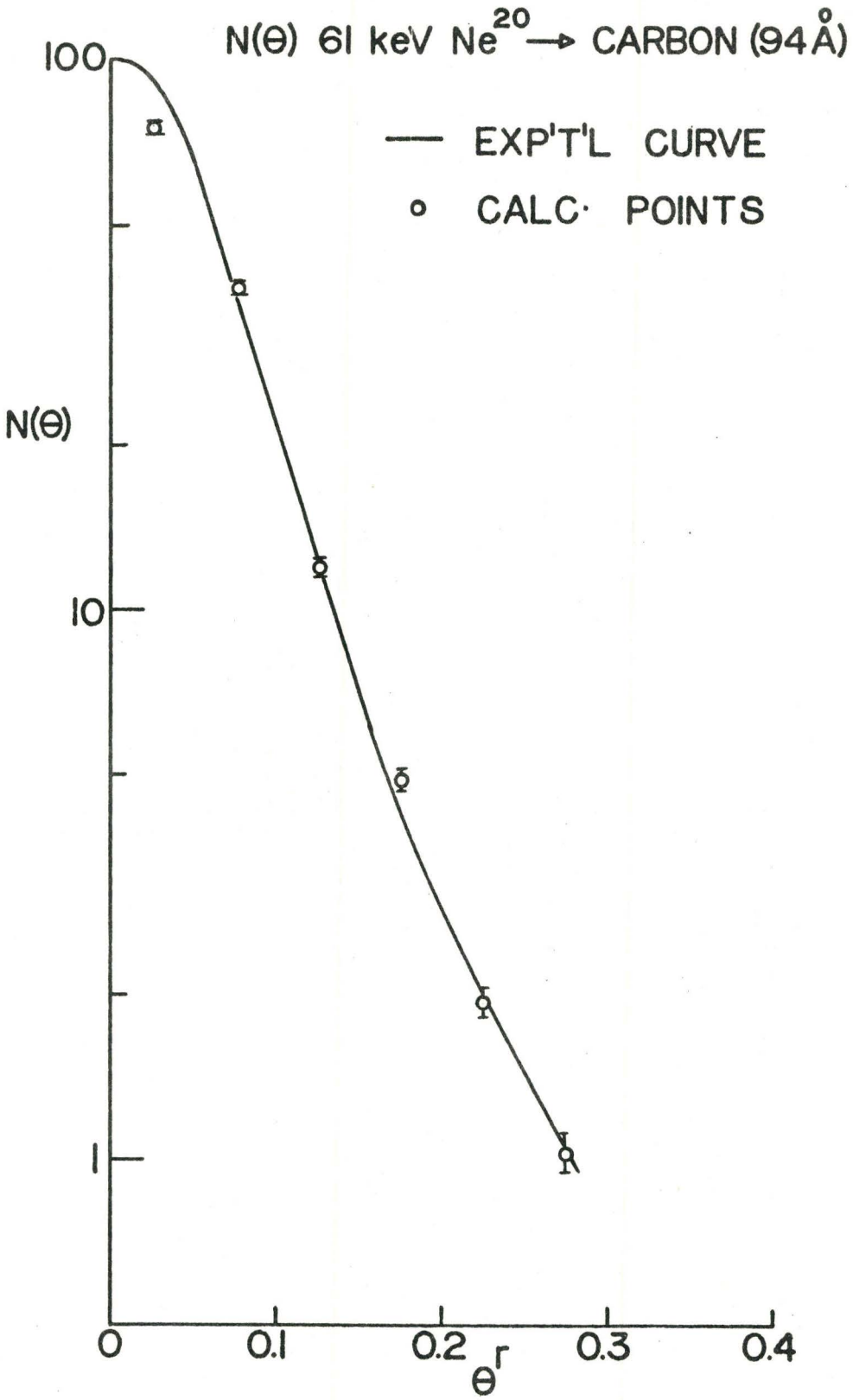
N(θ) 61 keV Ne20 → CARBON (94 Å)
EXP'T'L CURVE
CALC· POINTS
100
10
1
N(θ)
0
0.1
0.2
0.3
0.4
θr

FIG. 10.

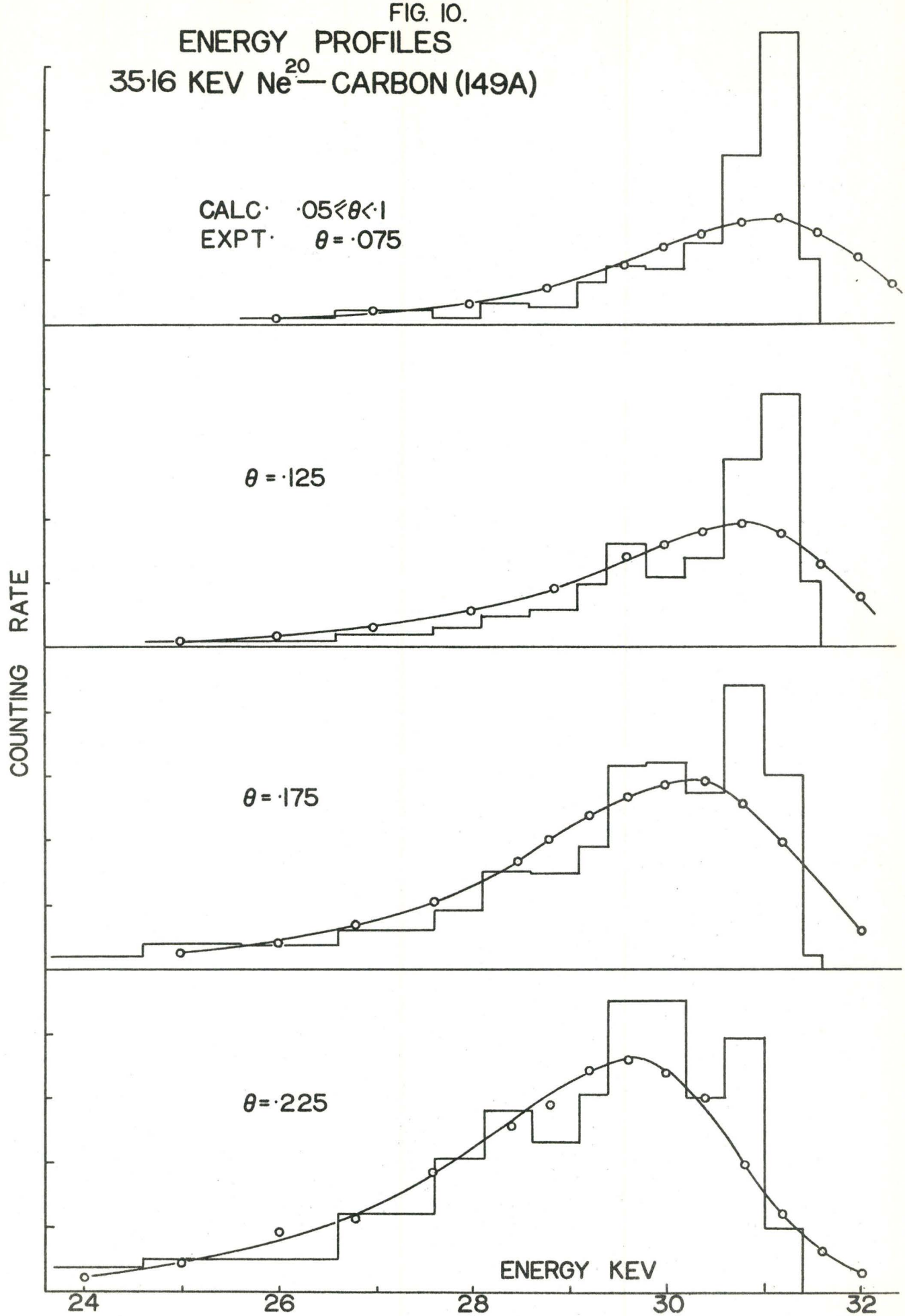
ENERGY PROFILES
35·16 KEV Ne20 — CARBON (149A)
CALC· ·05≤θ<·1
EXPT· θ = ·075
θ = ·125
θ = ·175
θ = ·225
COUNTING RATE
ENERGY KEV
24
26
28
30
32

CHAPTER IV

EXPERIMENTAL RESULTS

1. Hydrogen, Helium and Lithium.

These three elements form a natural grouping because, in the energy interval considered, the nuclear contribution to S_o is negligible; this results in the simplifying approximation that $S_o = S_\epsilon$. Although the nuclear contribution to S_o is negligible, the total nuclear stopping cross-section is not. For hydrogen, S_ν is two orders of magnitude below S_ϵ. For helium the total nuclear stopping cross-section at 10keV is 17% of S_ϵ and, of course, decreases as the energy increases. For lithium, S_ν and S_ϵ are of equal magnitude near 6keV.

The hydrogen and helium results are an extension of the relative measurements of Van Wijngaarden and Duckworth (V-62). The two sets of results display the same energy dependence in the region where they overlap.

The observed stopping cross-sections for hydrogen are shown in Figure 11. This curve represents an absolute determination of S_o since some of the experiments were performed with weighed films. (See Section II-2). This curve was used as a standard to measure the film thicknesses.

The hydrogen ions were produced with an electron bombardment source, using the residual water vapour in the ion source as the gas. This ready availability of

hydrogen ions was particularly convenient since it permitted the film thickness to be monitored, even when other samples were in the gas system.

The observed stopping cross-sections in carbon for He^4 are shown in Figure 12, and for the two lithium isotopes in Figure 13.

2. Beryllium, Boron, Carbon, Nitrogen, Oxygen, Fluorine, Neon, Sodium and Magnesium.

The stopping cross-sections in carbon for these atoms are shown in Figures 14 to 22. S_o cannot be associated directly with S_ϵ over the complete energy interval, as was the case with the lighter projectiles. The difference between S_o and S_ϵ was determined with the Monte Carlo calculation as outlined in Chapter III.

At any given energy, the nuclear stopping cross-section increases with increasing mass. The same is true for that portion of the nuclear stopping cross-section observed by the electrostatic analyzer. For all projectiles up to neon, the Monte Carlo correction is quite small near the upper energy limit, and the coefficient for the electronic stopping cross-section (Equation III-2) is almost completely determined by the experiment alone. For sodium, however, where doubly-charged ions were not used, a correction of $\sim$15% was found at the highest energy studied.

Three curves are drawn for each atom studied. The observed stopping cross-sections are shown for a

particular carbon film. The electronic cross-sections shown are determined from the observed stopping cross-sections with the corrections from the Monte Carlo calculation. The nuclear stopping cross-sections are from the theoretical predictions of Lindhard et al (L-61a). These are just explicit solutions of the universal curve shown in Figure 1. To minimize crowding on the graphs, the total stopping cross-sections are not plotted.

3. Summary.

The experiments were performed on at least two films for each of the atomic projectiles studied. In isolated instances, a set of results disagreed by as much as 3% with the final value adopted for the stopping cross-sections.

The results for the electronic stopping cross-sections are tabulated below, assuming an equation of the form

$$S_\epsilon = kE^P \quad eV\text{-}cm^2/atom \qquad \ldots \text{(IV-1)}$$

where E is expressed in kilovolts. The values for k and P are the averages of several sets of data.

TABLE IV-1

Atom	$kx10^{15}$	P	Energy Interval (keV)
H^1	3.3	.40	10-25
He^4	3.7	.43	10-80
Li^6	3.0	.45	20-70
Li^7	3.0	.43	15-70
Be^9	3.3	.48	12-130
B^{11}	4.4	.47	12-140
C^{12}	5.9	.43	12-140
N^{14}	6.2	.44	15-140
O^{16}	6.2	.42	20-140
F^{19}	4.9	.45	20-140
Ne^{20}	3.8	.47	20-140
Na^{23}	2.9	.48	20-70
Mg^{24}	2.5	.50	20-130

OBSERVED STOPPING CROSS-SECTIONS

$H^1 \rightarrow$ CARBON

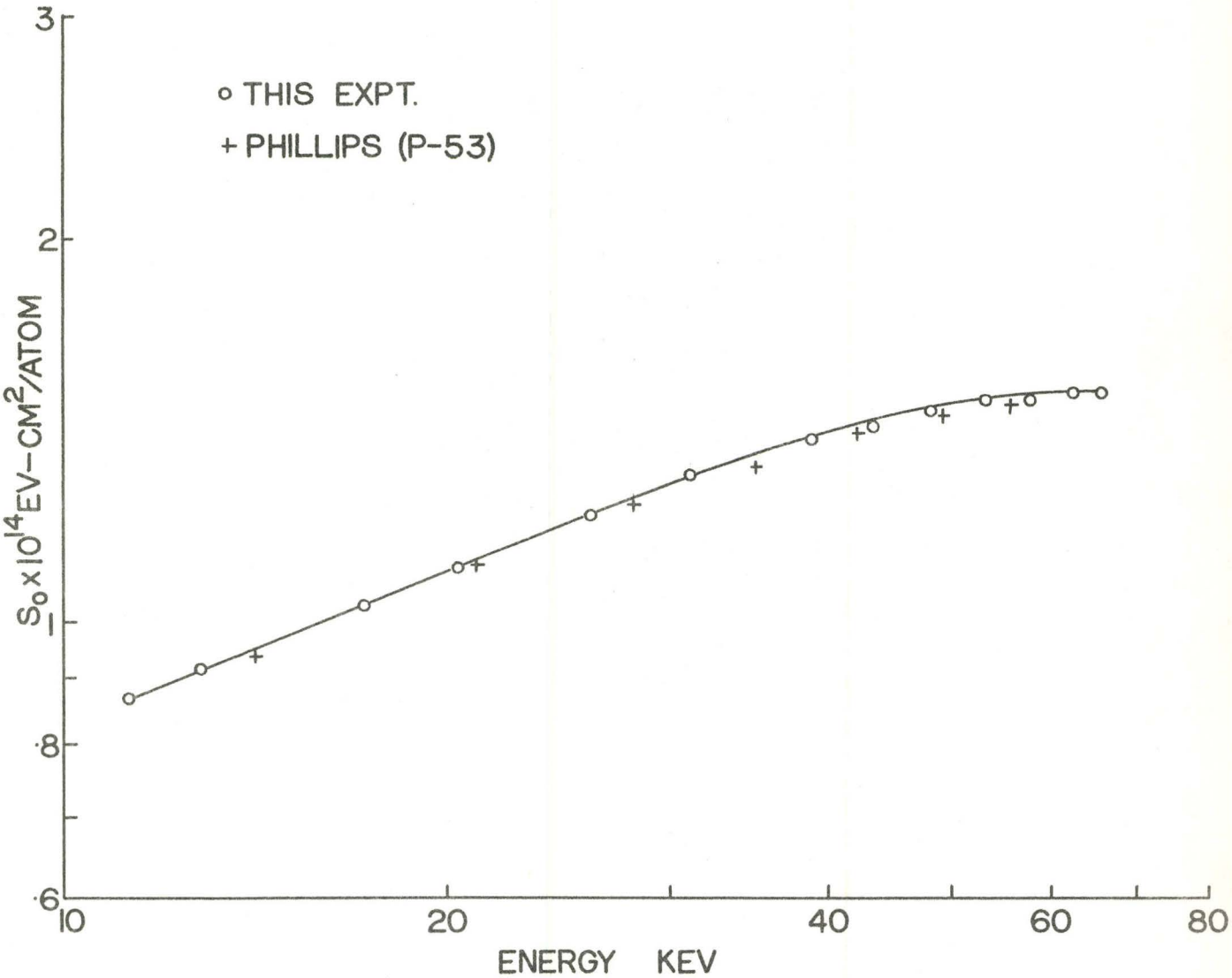

FIG. II.

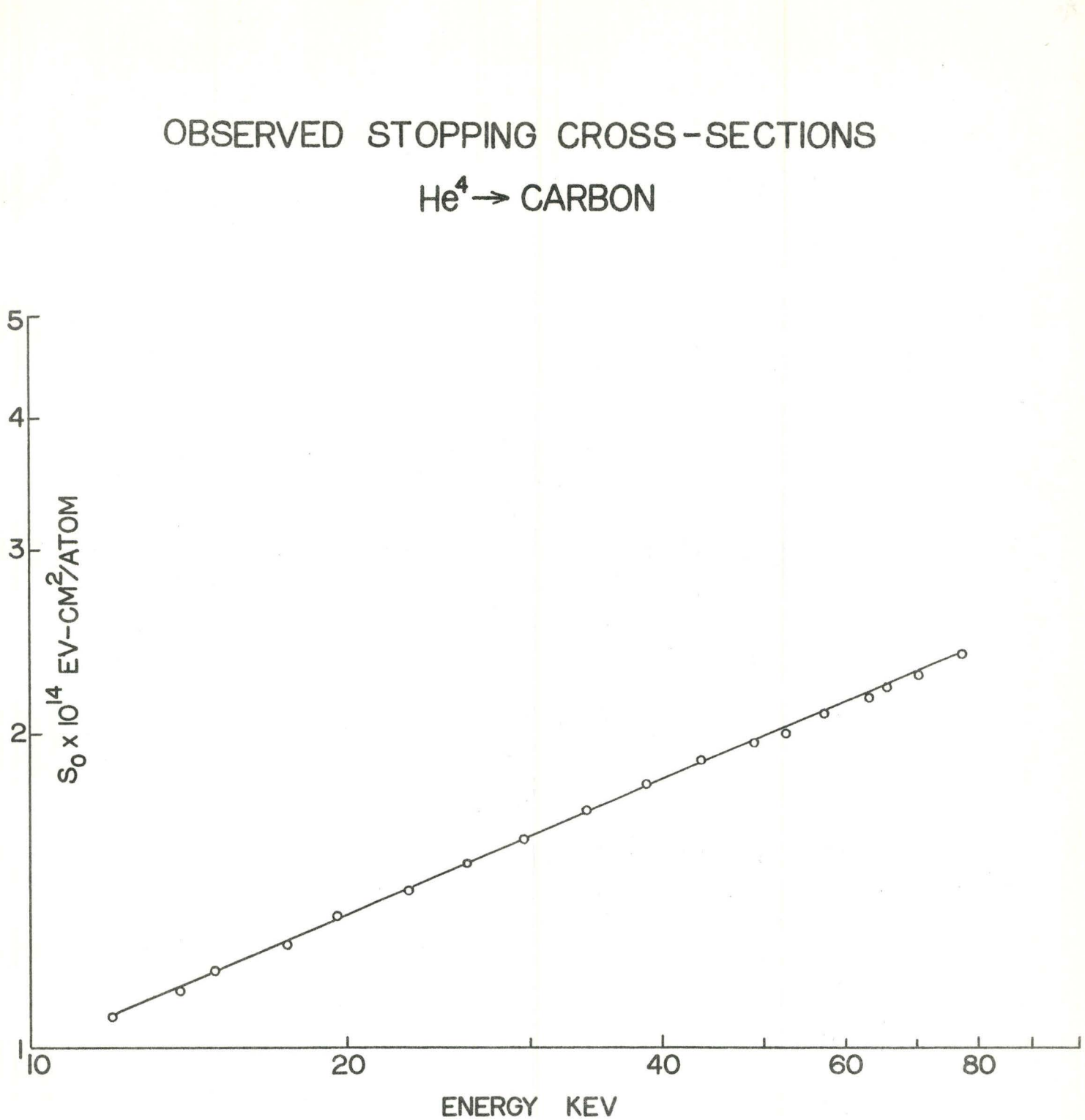
OBSERVED STOPPING CROSS-SECTIONS
He⁴ → CARBON
5
4
3
2
1
S₀ x 10¹⁴ EV-CM²/ATOM
10
20
40
60
80
ENERGY KEV

FIG. 12.

OBSERVED STOPPING CROSS-SECTIONS

Li → CARBON

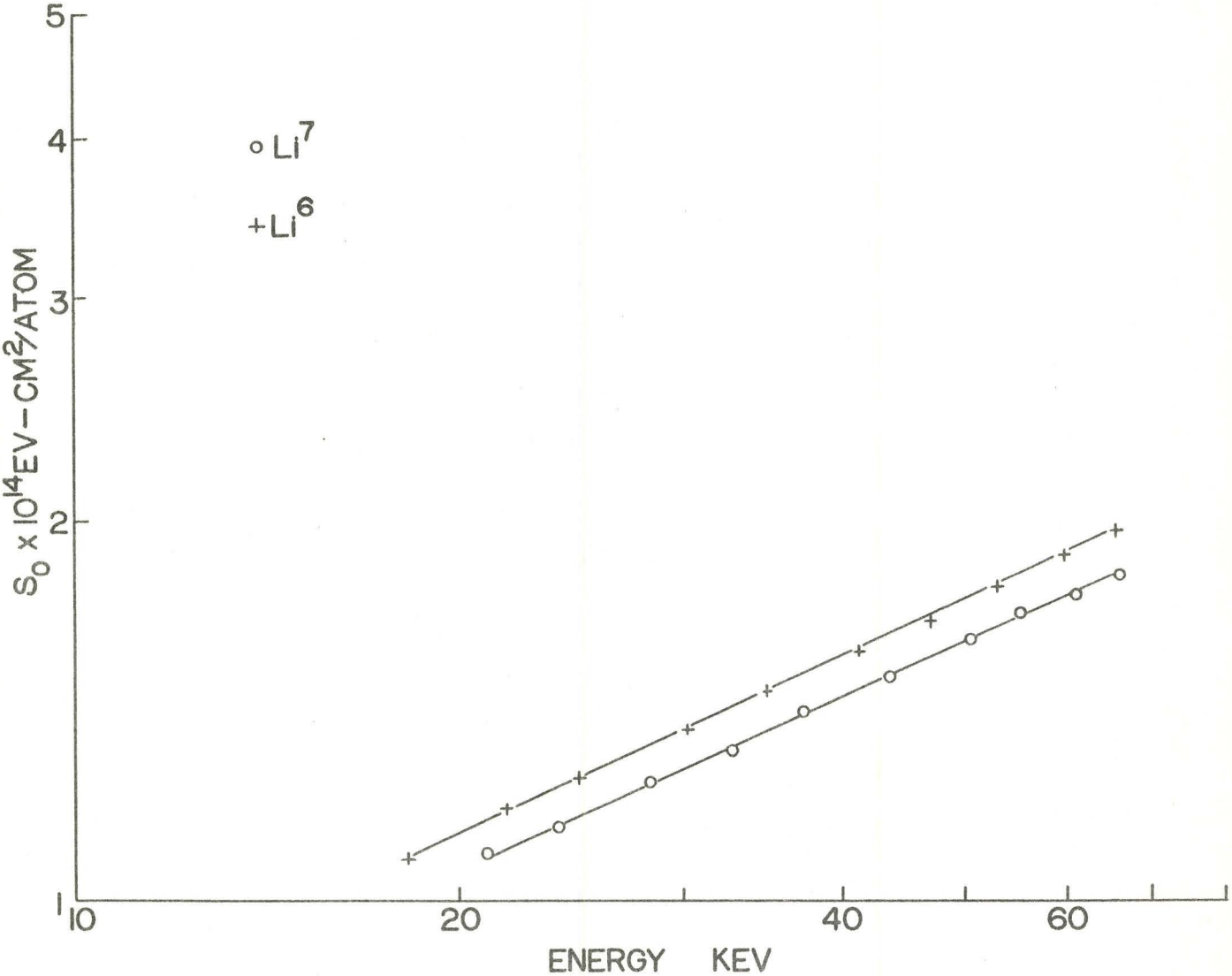

FIG. 13.

STOPPING CROSS-SECTIONS
$Be^{9} \rightarrow$ CARBON

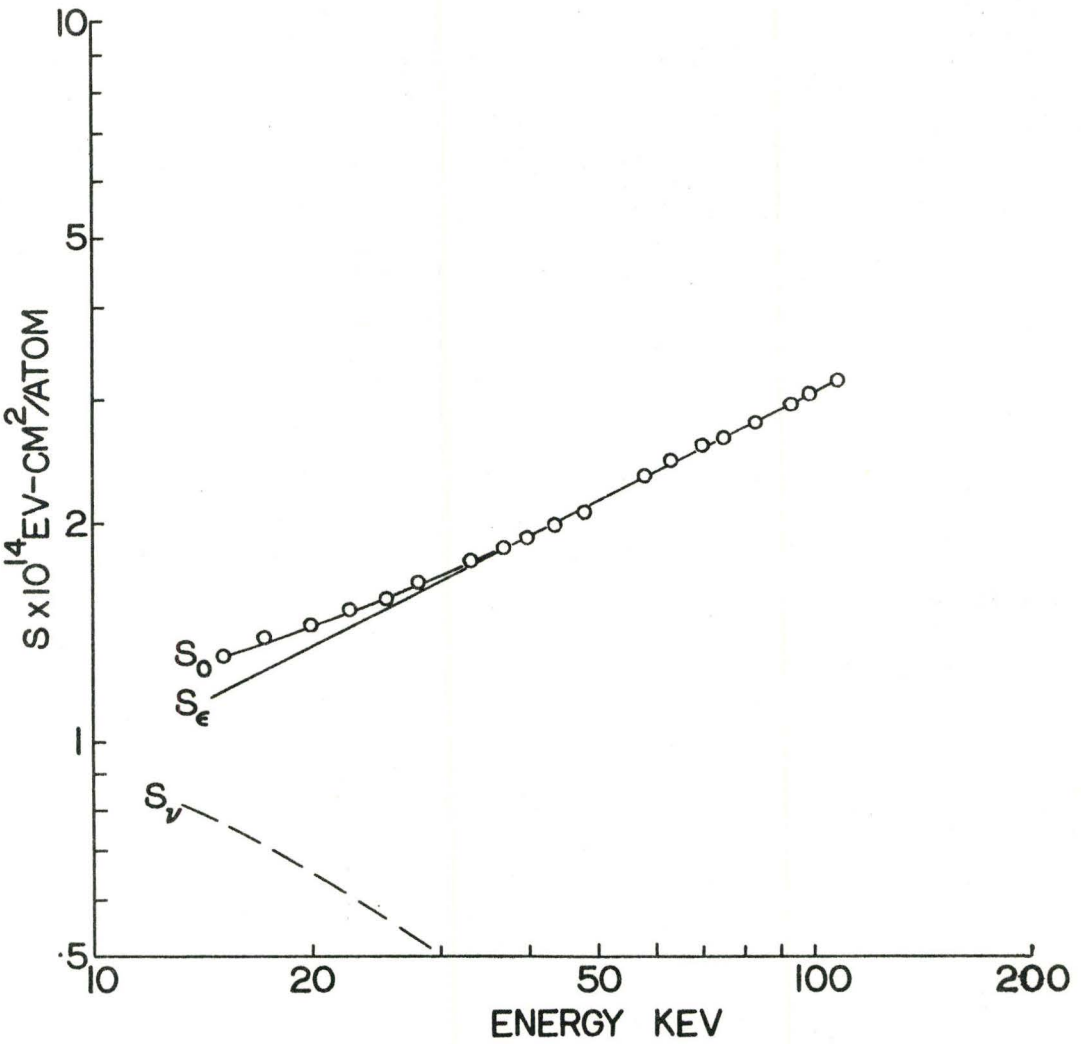

FIG. 14.

STOPPING CROSS-SECTIONS

$B^{11} \rightarrow$ CARBON

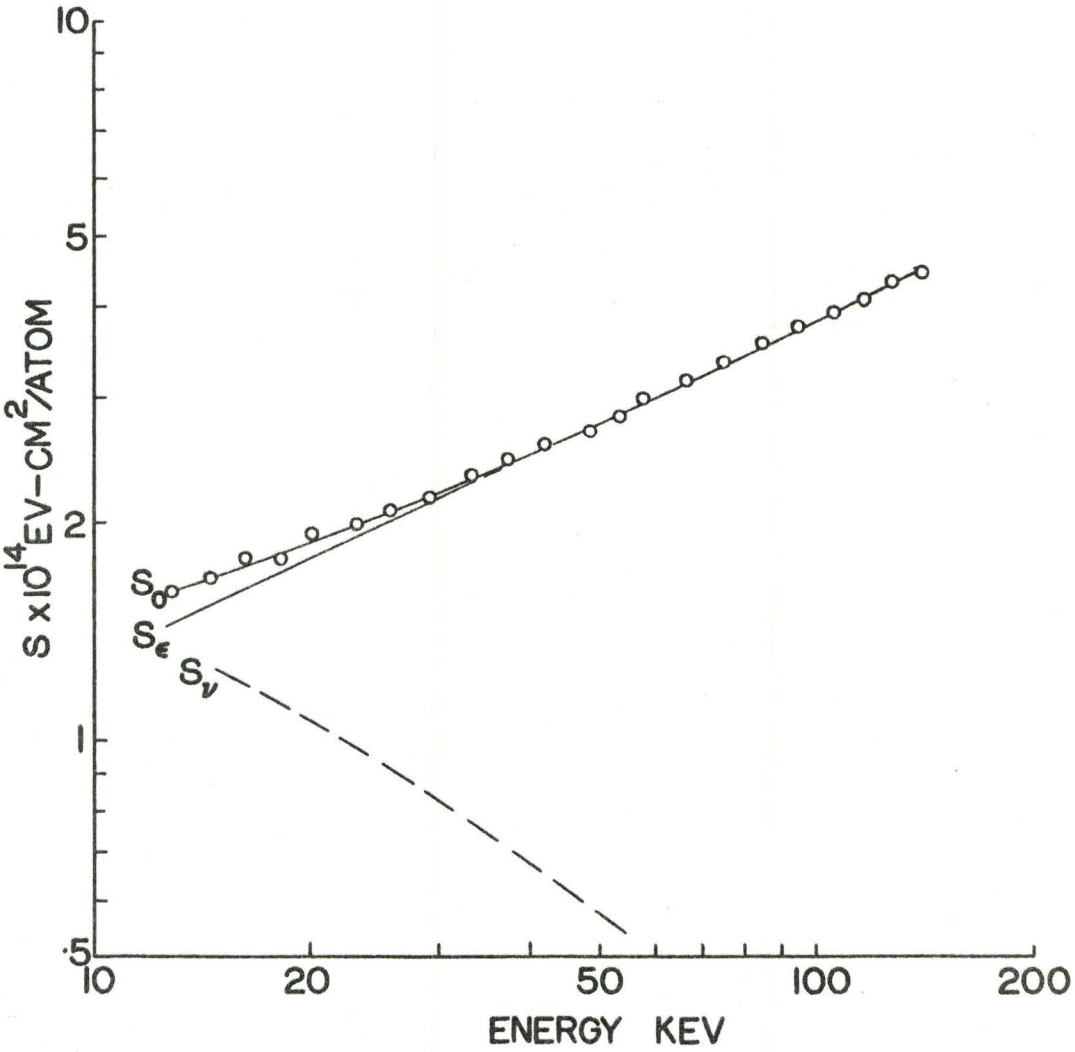

FIG. 15.

STOPPING CROSS-SECTIONS

$C^{12} \rightarrow$ CARBON

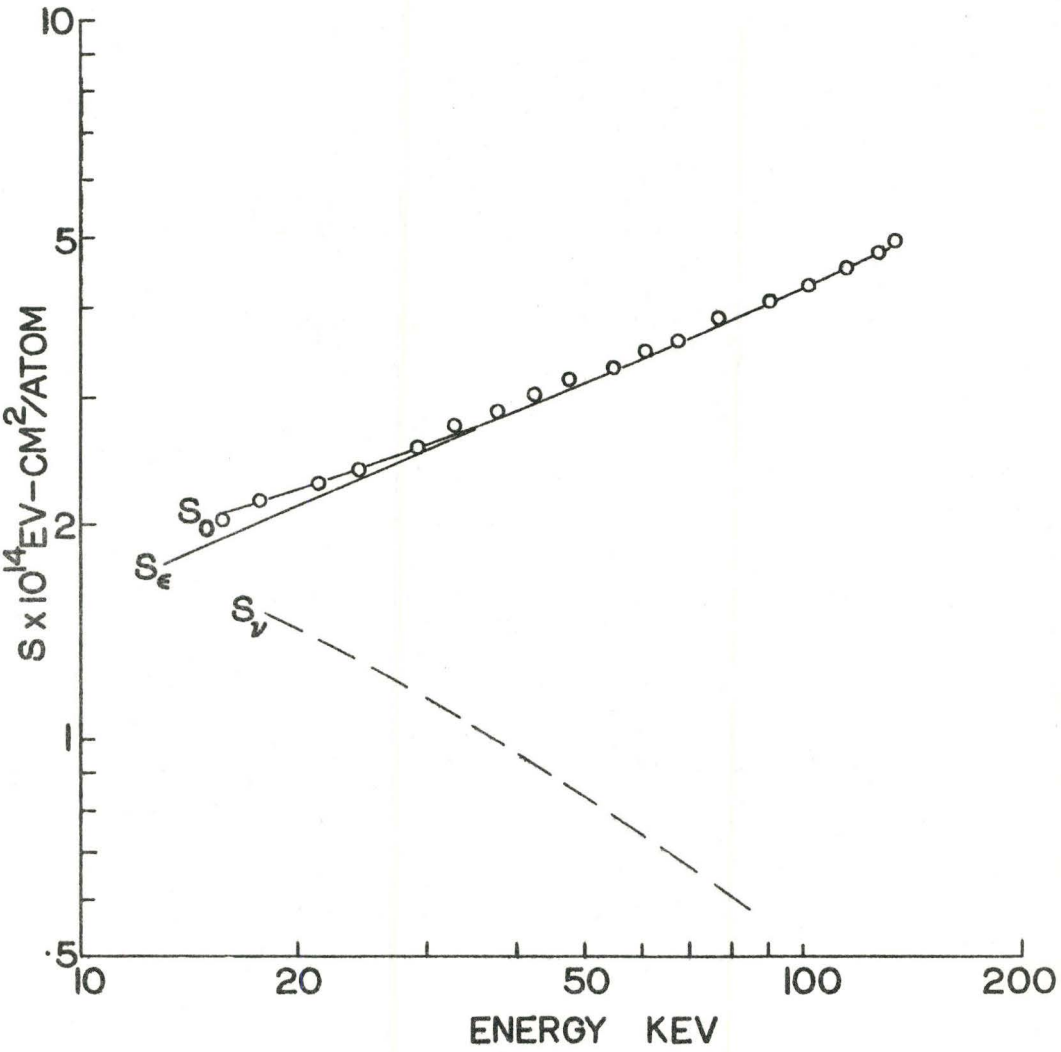

FIG. 16.

STOPPING CROSS-SECTIONS
$N^{14} \rightarrow$ CARBON

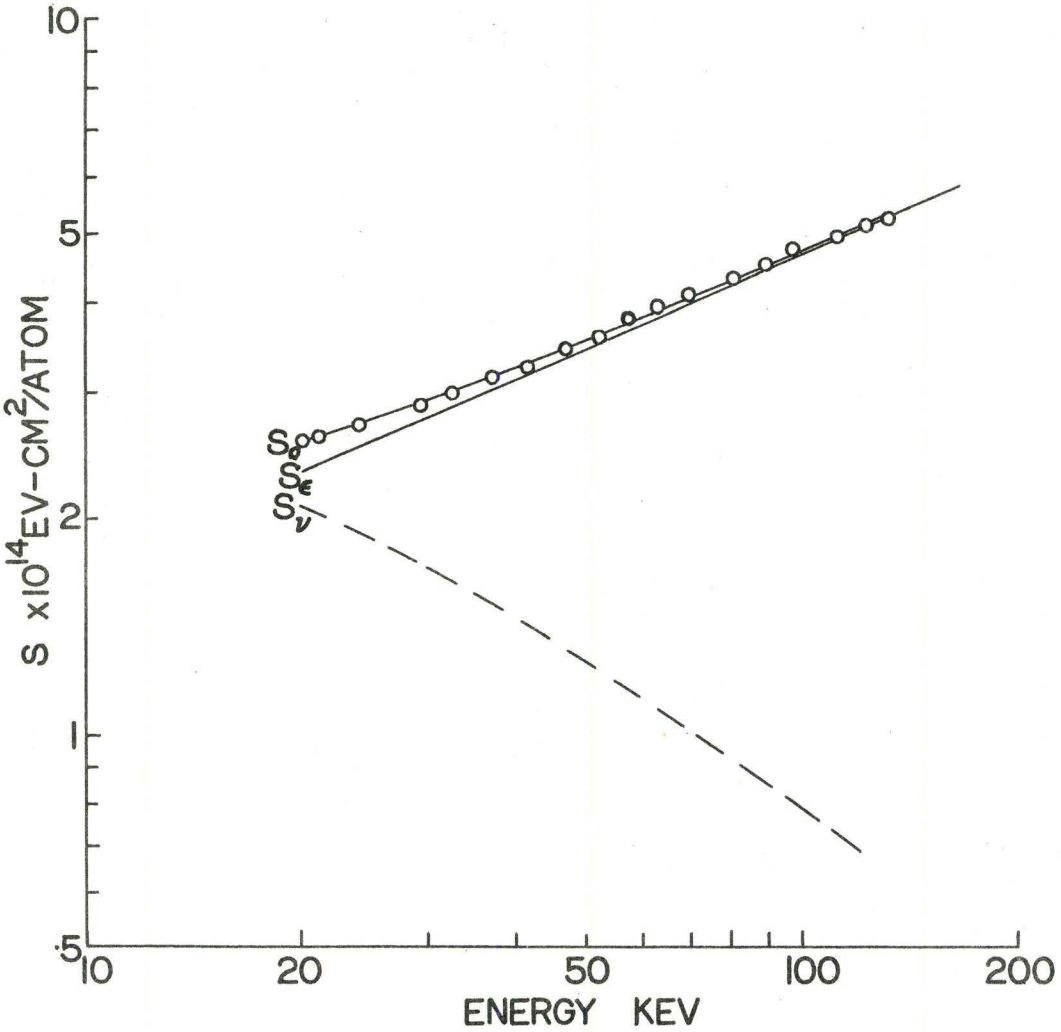

FIG. 17.

STOPPING CROSS-SECTIONS
$O^{16} \rightarrow$ CARBON

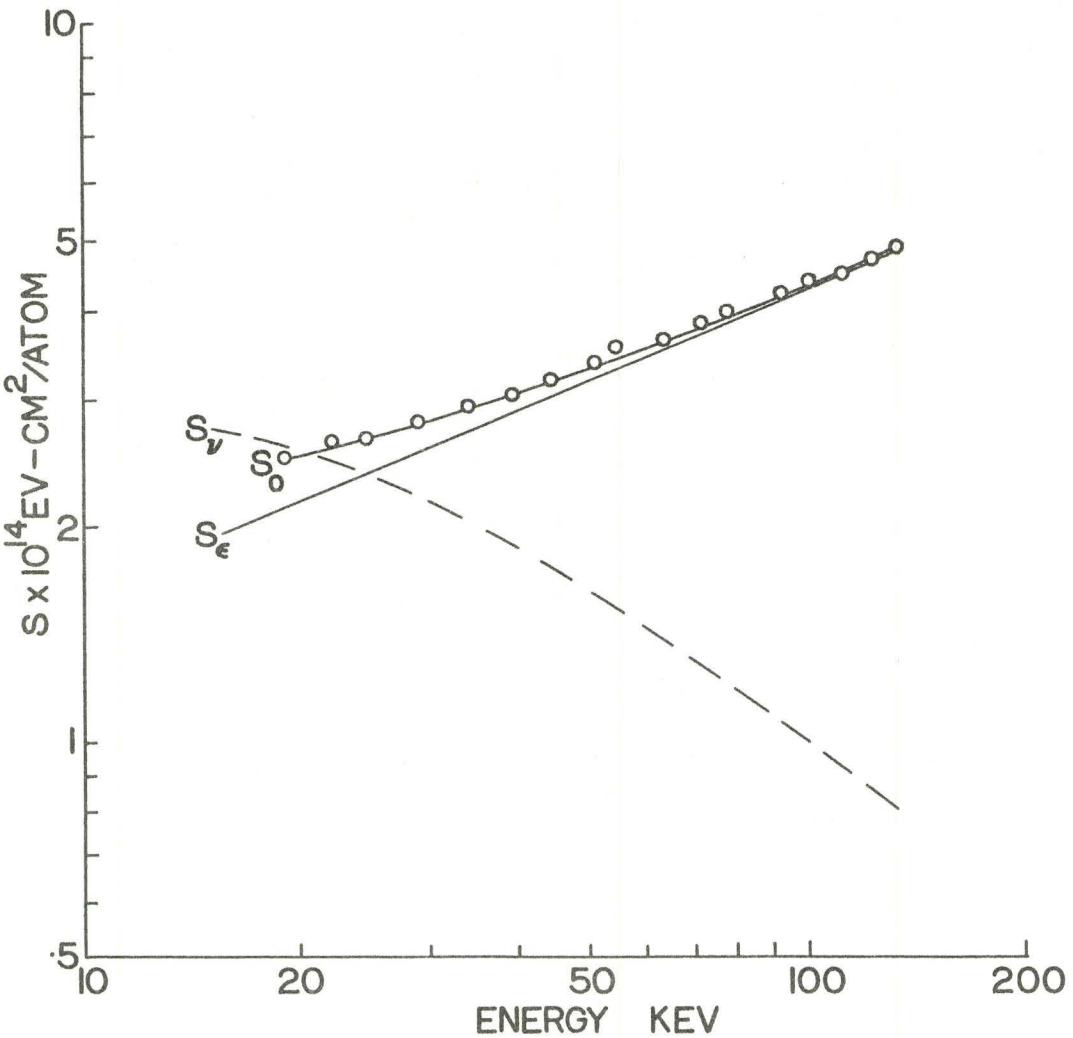

FIG. 18.

STOPPING CROSS-SECTIONS
$F^{19} \rightarrow$ CARBON

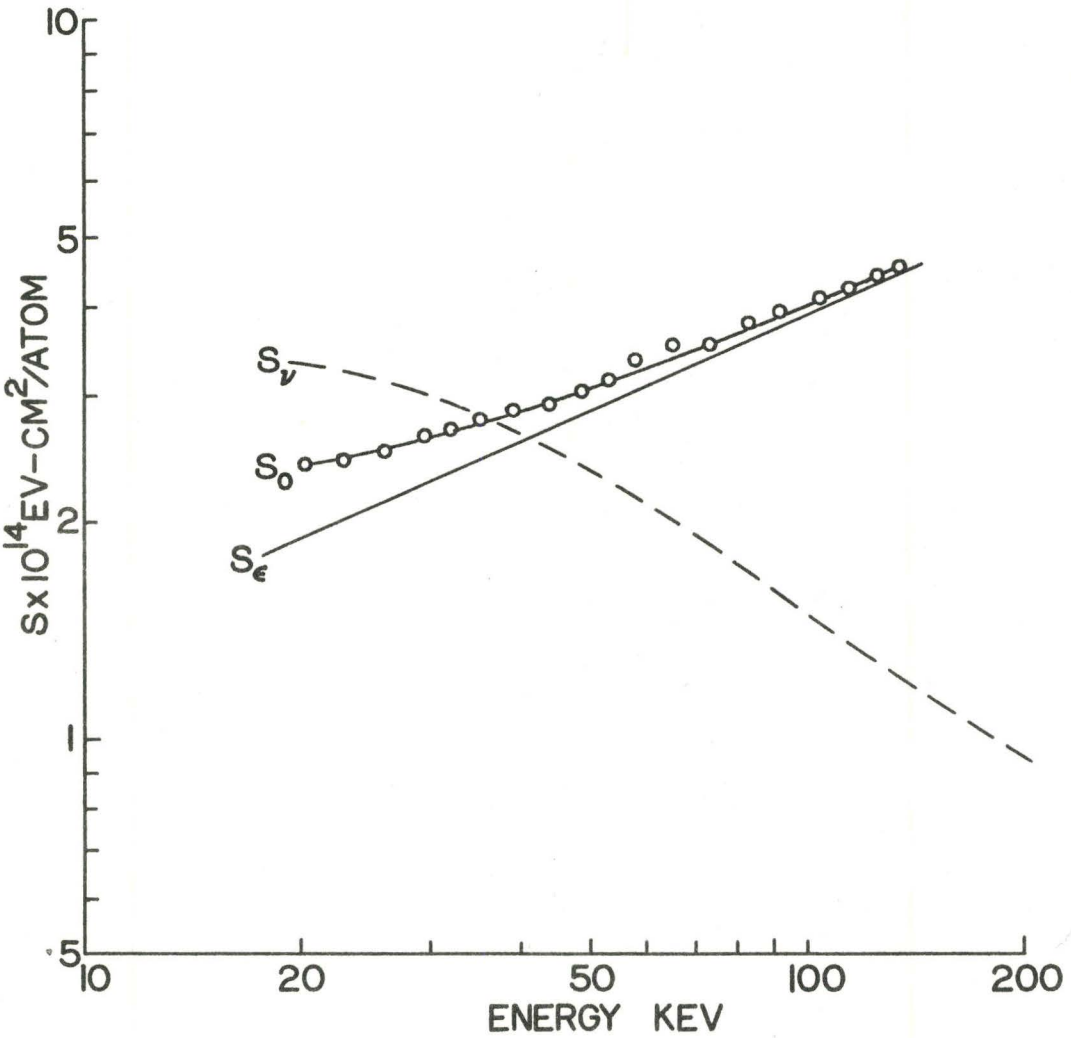

FIG. 19.

STOPPING CROSS-SECTIONS
$Ne^{20} \rightarrow$ CARBON

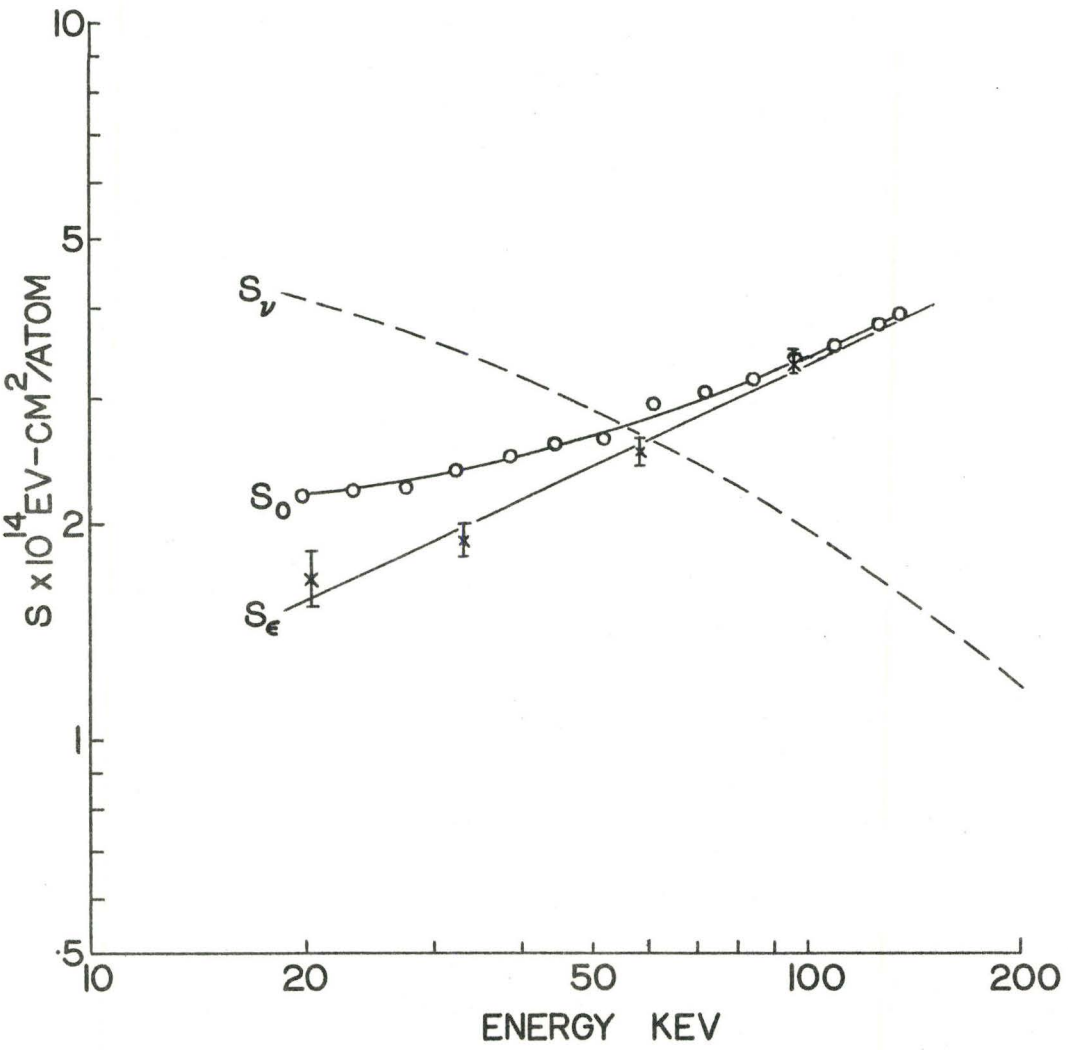

FIG. 20.

STOPPING CROSS-SECTIONS
$Na^{23} \rightarrow$ CARBON

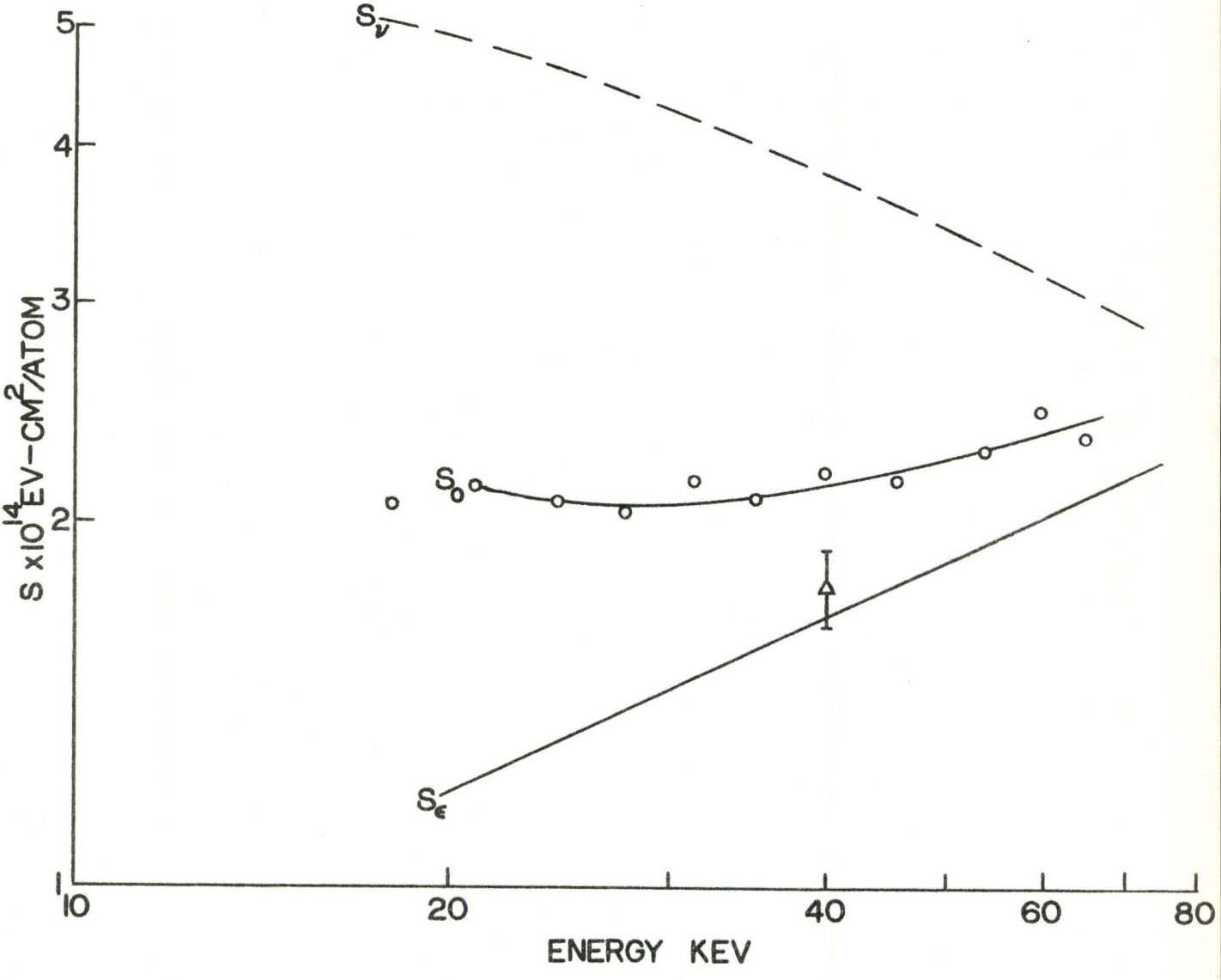

FIG. 21.

STOPPING CROSS-SECTIONS

$Mg^{24} \rightarrow$ CARBON

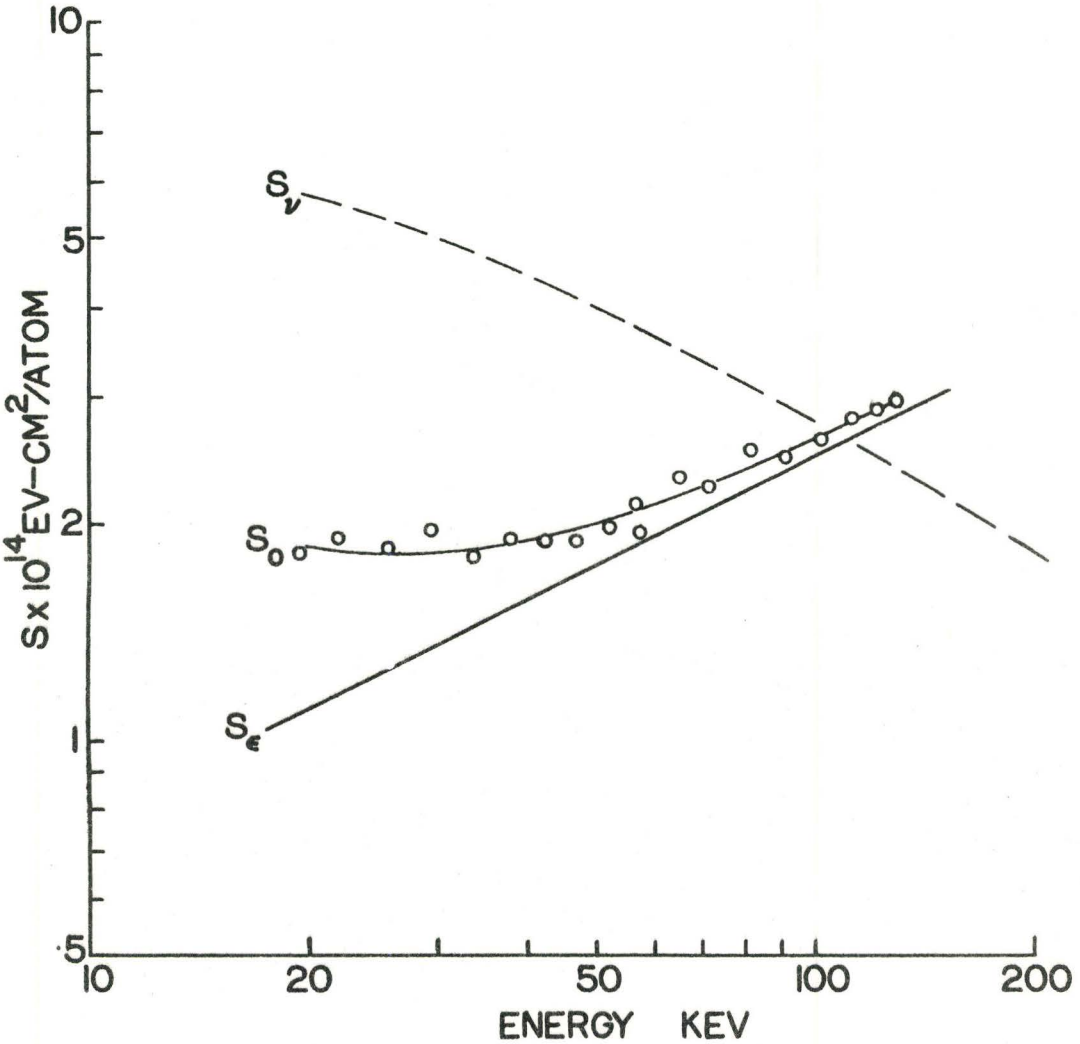

FIG. 22.

CHAPTER V

DISCUSSION AND CONCLUSIONS

1. Comparison with Other Experiments

The existing data on stopping cross-sections in this energy interval are meagre and only three comparisons are available. Furthermore, these comparison results differ in nature from the present ones in that they are either range measurements or stopping cross-sections measured with gaseous targets. Two of these comparisons will be made now, and the third later.

Phillips (P-53) has reported the electronic stopping cross-sections for protons in carbon in the energy interval $10 < E < 80$keV. He measured the energy loss of protons passing through a gas cell enclosed by thin SiO windows. The geometry of the experiment was such that only the electronic stopping cross-section was measured.

The stopping effect of carbon was not measured directly, but found from the stopping characteristics of CO_2 and O_2, assuming the stopping power of a molecule to be equal to the sum of the stopping powers of the constituent atoms. To justify this assumption in this energy interval, the stopping power for water vapour was compared with the stopping power calculated for hydrogen and oxygen. The agreement was good.

There are reasons for not placing too much

emphasis on the comparison between the present results and those of Phillips. Whaling (W-58) is reluctant to accept Phillips' values in view of their disagreement with measurements made at higher energies. One might also object to a comparison of stopping cross-sections obtained in one case from a gas and in the other from a solid (P-53). Nevertheless, both sets of results are plotted in Figure 11. They agree everywhere within 2%.

We may also compare our results with the range measurements of Powers and Whaling (P-62). Their results include the ranges of nitrogen and neon in carbon. Their experiment consisted of bombarding the carbon target with ions of the projectile under consideration, and then bombarding the target with protons in order to scatter them elastically from the atoms now imbedded in it. The protons were momentum analyzed at a laboratory scattering angle of 129°. For a given analyzer setting, the incident proton energy was varied and the resulting profile of the elastically scattered protons recorded. Using the known stopping power for protons in the target material and the mass of the imbedded scattering centres, the range of the latter in the target was computed.

Since we do not know the stopping powers down to zero energy, we cannot obtain ranges from our data. We can, however, obtain range differences. To determine the range difference ($\triangle R$) for two energies from our data,

the total stopping cross-section must be integrated, viz.,

$$\Delta R = \frac{1}{N} \int_{E_1}^{E_2} S_t^{-1} dE \qquad \ldots \text{(V-1)}$$

Normally, such an integration must be performed numerically. A considerable simplification is introduced if one approximates S_t by an equation of the form

$$S_t = kE^P \qquad \ldots \text{(V-2)}$$

If such an equation does not fit the range of energy required, one can break the differential stopping curve into energy intervals and fit such an equation to each interval. Allowing such a form for S_t, the integral in Equation V-1 can be easily solved to yield

$$\Delta R = \frac{1}{kN(1-P)} \left(E_2^{(1-P)} - E_1^{(1-P)} \right) \qquad \ldots \text{(V-3)}$$

The result of such an integration yields the range difference, while an experimental range difference determination measures differences in the <u>projected</u> range. The difference arises from the increased path length traced out by the projectile on the crooked trajectory caused by nuclear collisions. We have ignored this correction but we shall compare only the

range differences above 50keV, thus eliminating the energy interval where the correction is most important. Both sets of results are listed in Table V-2. For both nitrogen and neon we have extrapolated S_ϵ from 140keV to 200keV to permit the comparison to be made at the higher energy. The values for k and P used to describe S_t are listed in Table V-1. The coefficient k displays what might appear to be a marked discontinuity in S_t at 100keV. For nitrogen at 100keV with k = 1.0 and P = .22, Equation V-2 yields S_t = 2.75keV $cm^2/\mu g$, while using k = .62 and P = .32, S_t = 2.71keV $cm^2/\mu g$, a difference of less than 1.5%.

The range differences determined by the two experiments agree everywhere within the experimental error. The effect of the projected range should be negligible in all except the 50-100keV Ne results, where it would tend to increase somewhat the small discrepancy between the results listed in Table V-2. It should be noted that our nitrogen range differences are derived much more from experimentally measured quantities than are the corresponding values for neon. For example, at 100keV, S_ν (from Lindhard's calculation) accounts for 13% of S_t for N^{14} and 37% of S_t for Ne^{20}. We have not quoted errors in the range differences calculated from our experimental results since the total stopping cross-sections include the theoretical S_ν values. Where the total stopping cross-sections are due mainly to our

results, the errors are of the order of 5%.

TABLE V-1

Projectile	Energy Interval (keV)	k ($keV cm^2/\mu g$)	P
N^{14}	50-100	1.0	.22
N^{14}	100-200	.62	.32
Ne^{20}	50-100	2.6	0
Ne^{20}	100-200	1.4	.15

TABLE V-2

Projectile	Energy (keV)	Range(P-62) ($\mu g/cm^2$)	ΔR(P-62) ($\mu g/cm^2$)	ΔR(This exp't) ($\mu g/cm^2$)
N^{14}	49.9	24.0 ± 3.6	19.4	19.5
	99.7	43.4 ± 3.2	32.3	33.0
	199.6	75.7 ± 6.7		
Ne^{20}	50.1	17.9 ± 2.1	20.4	18.9
	99.6	38.3 ± 2.7	36.9	35.0
	200.2	75.2 ± 4.1		

2. Comparison with Theory.

Although we did not attempt a detailed study of the nuclear stopping cross-sections, our $N(\theta)$ measurements afford a somewhat crude comparison with the theory. A study of the nuclear stopping process would be best achieved by a study of the differential scattering cross-sections, and the nuclear stopping cross-sections would follow with the aid of Equation I-6.

The $N(\theta)$ distributions are the result of multiple collisions, and, of course, are no substitute for the single collision type of measurement. However, the Monte Carlo calculation acts as a bridge between the two and it is apparent in Figures 8 and 9 that the differential cross-section proposed by Lindhard *et al* (L-61a) agrees well with the experimental results.

Besides the Ne^{20} results, calculations and experiments were also performed for A^{40} at 50 and 100keV, and for Kr^{84} at 64keV. These situations correspond to b/a values of 0.8, 0.4 and 3 respectively. In all these cases, the calculated and experimental $N(\theta)$ results agreed quite well.

For these heavier ions, it was found that the $N(\theta)$ curve was more sensitive to the discriminator setting of the counting equipment. For higher discriminator settings, the counting rate was relatively smaller at the larger scattering angles. This suggests a lower average pulse height at these angles, a fact verified visually with an oscilloscope. This effect could well be caused by the fringing field of the magnet. To minimize such effects, the electron multiplier was housed in a soft iron jacket and the whole $N(\theta)$ apparatus mounted on an extension as far from the magnet as beam intensity would allow. At the higher magnetic fields required for these heavier ions, however, these precautions may not have been sufficient.

In general, the agreement between the theory governing S_ν and our experiment is good. It must be realized, however, that this experimental confirmation is only a rough one.

Our determination of S_ϵ was considerably more accurate than S_ν, and we can make a much more critical comparison with the theory.

Hydrogen was the only projectile studied beyond the velocity limit of the theory of Lindhard and Scharff (L-61). They predict S_ϵ to be directly proportional to the velocity up to 25keV (see Equation I-8). Beyond this energy, S_ϵ should approach a maximum and then decrease with increasing energy according to the Bethe stopping formula. Our experiments indicate that such a maximum has been reached at approximately 70keV (see Figure 11).

Equation I-8 predicts that when different isotopes have the same velocity, their electronic stopping cross-sections should be equal. This prediction was experimentally verified with the lithium isotopes. As a more illustrative representation of this isotope effect, we have plotted the observed stopping cross-sections of both Li^6 and Li^7 against velocity. This plot is shown in Figure 23 where the two sets of results do lie on a common curve. Phillips (P-53) also found such a velocity dependence for the hydrogen isotopes in various stopping gases.

There are two points to consider in comparing the main body of our data to the theoretical electronic stopping cross-sections expressed by Equation I-8. First, there is the velocity dependence and second, the coefficient's Z dependence. Again, one might object to applying the Thomas-Fermi arguments implicit in Equation I-8 to low Z projectiles. However, Equation I-8 represents the only treatment available on electronic stopping in this energy interval, and the results should be at least indicative of the Z dependence.

The energy dependence for the projectiles is listed in Table IV-1. The exponents (P) range from 0.40 to 0.50, whereas a velocity dependence would have an exponent (P) of 0.50. In the light of the model used, the agreement must be regarded as quite reasonable.

A graphical comparison of the experimental and theoretical electronic stopping cross-sections as a function of Z_1 is shown in Figure 24. The velocity used (9×10^7 cm/sec) has no particular significance. It was chosen because all projectiles except H^1 and Na^{23} were studied at this velocity. The values used for H^1 and Na^{23} are extrapolations using Equation IV-1 and the coefficients and exponents listed in Table IV-1. In the case of hydrogen, we know from previous work

(V-62) that the extrapolation is valid. For sodium, our only justification is that adjacent ions continue to higher energies in the manner expressed by Equation IV-1, and it is not unreasonable to expect the same of sodium.

The three lines drawn on the graph are the theoretical values of Lindhard and Scharff (L-61) corresponding to ξ_ϵ values of 1, $Z^{1/6}$ and 2, respectively. All of the atoms studied with the exception of N^{14} fall within the probable limits, i.e. $1 < \xi_\epsilon < 2$.

Taking the central ($\xi_\epsilon = Z^{1/6}$) theoretical curve as a base line, one sees that the theoretical stopping cross-sections proposed by Lindhard and Scharff certainly predict the trend of the experimental results. There is, however, the additional feature of a superimposed periodic dependence on Z. This difference betweeen the experimental and theoretical values of S_ϵ is not surprising. One would not expect a treatment based on Thomas-Fermi arguments to show any effects attributable to an atom's electronic structure because of the model's statistical nature. On the other hand, the outer electrons in the atoms will greatly affect the electronic stopping at these energies and one would expect the latter to display a corresponding periodicity. It is just this type of periodicity that is displayed by these results.

A non-monotonic dependence on Z_1 of the ranges in air of light atomic projectiles has been observed by Teplova et al (T-62). The minimum velocity used in their experiments was 2.6×10^8 cm/sec (above the adiabatic limit). They found range maxima at $Z_1 = 3$-4 and $Z_1 = 11$-13, which correspond roughly to minima for S_ϵ in our experiments. At greater velocities, they found the ranges became more monotonic with Z_1, indicating that the electronic structure for an individual atom becomes less important at higher velocities.

As stated previously, the electronic stopping cross-section is the conglomeration of all the inelastic processes occurring in the film. Consider charge exchange alone. Lindhard (L-54) states that the theoretical treatment includes charge exchange to the extent that such a phenomenon can be described by linear field equations. However, in this energy interval, it is the last electron (or two) which participates in the charge exchange process - the electron that displays the greatest periodic dependence. One would not expect a Thomas-Fermi treatment to reveal any effects due to the binding of these last electrons. An explanation of the details of this periodicity , including the positions of the minima, will presumably take into account the several charge states that a

projectile assumes during its passage through the film.

In summary, the theoretical analysis of Lindhard and Scharff (L-61) adequately predicts the electronic stopping within the limits imposed by the model used.

3. Conclusions.

The observed stopping cross-sections in thin carbon films for atomic projectiles with $Z \leq 12$ have been measured in the forward direction for energies ranging from 10 to 140keV.

An absolute measurement of the electronic stopping cross-sections for protons in carbon has been made. This result is used to determine the thickness of the films used in the experiments.

A Monte Carlo calculation has been developed to determine the extent that nuclear collisions affect the observed stopping cross-section. This permits the separation of the electronic stopping from the observed stopping by subtracting the nuclear component. The electronic stopping cross-sections so determined are listed in Table IV-1.

The results have been compared with the theoretical analysis of Lindhard and Scharff (L-61). The agreement between their predictions and our results is good. One feature of the experimental electronic stopping cross-sections not predicted by the theory is a periodic Z dependence.

OBSERVED STOPPING CROSS-SECTIONS

Li → CARBON

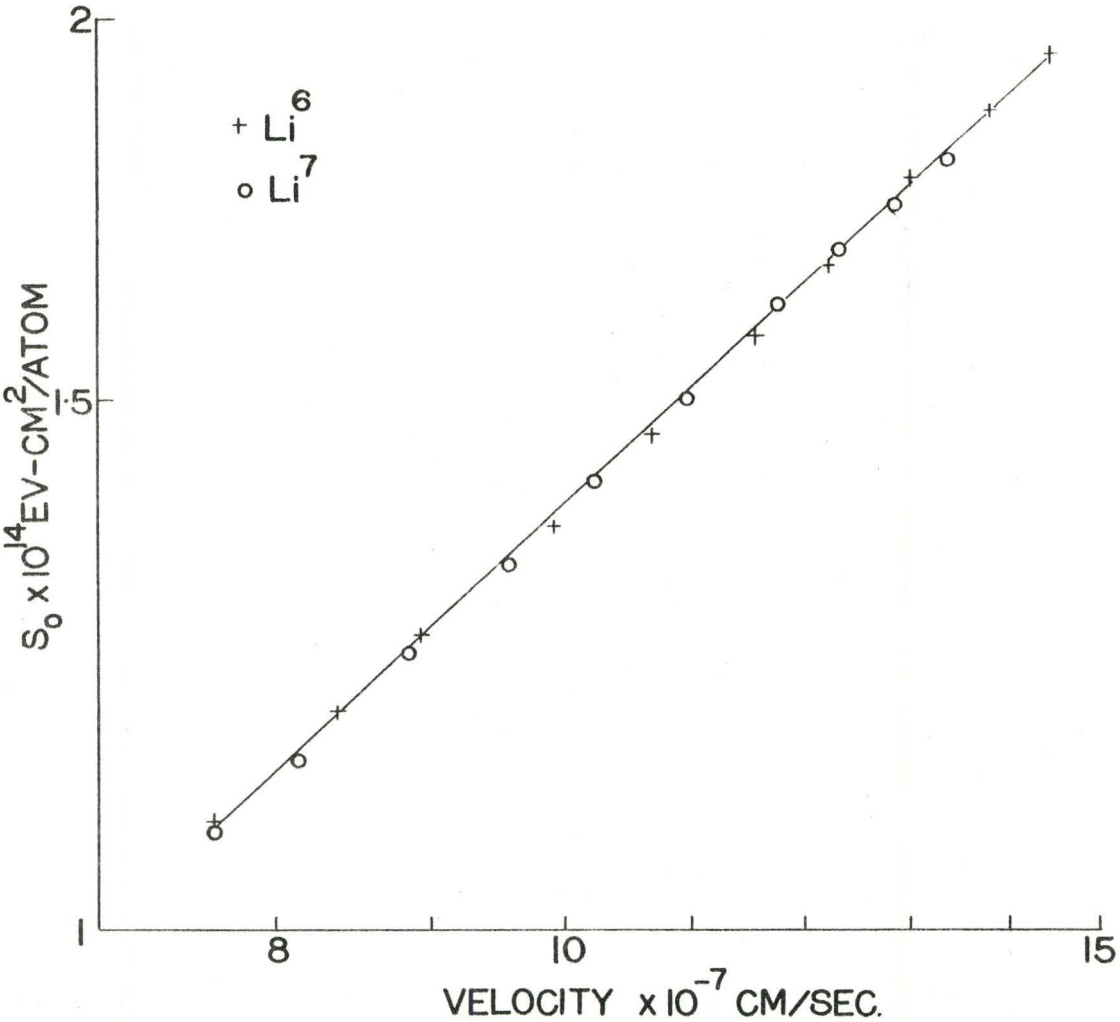

FIG. 23.

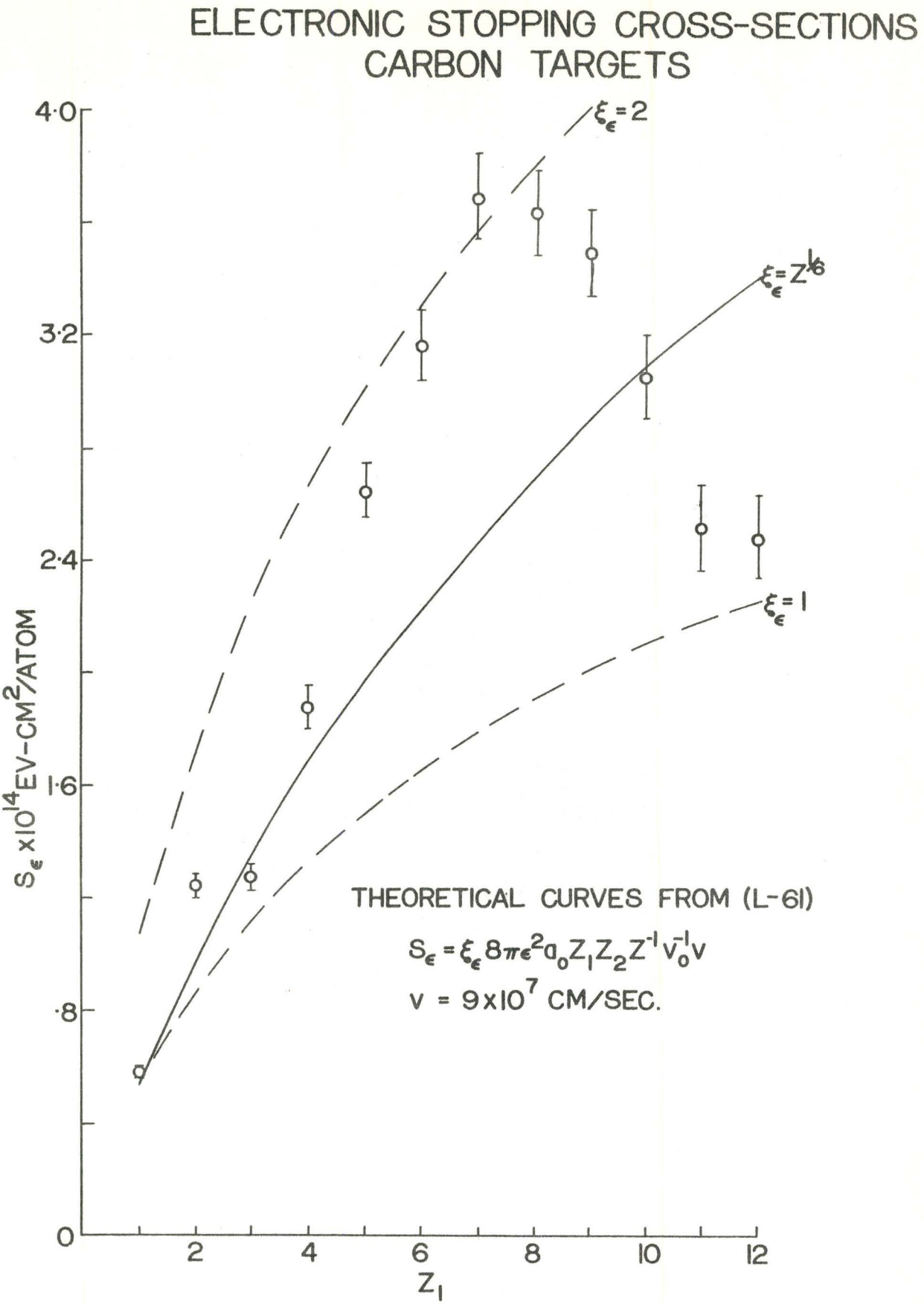
ELECTRONIC STOPPING CROSS-SECTIONS
CARBON TARGETS
$\xi_\epsilon = 2$
$\xi_\epsilon = Z^{1/6}$
$\xi_\epsilon = 1$
THEORETICAL CURVES FROM (L-61)
$S_\epsilon = \xi_\epsilon 8\pi\epsilon^2 a_0 Z_1 Z_2 Z^{-1} v_0^{-1} v$
$v = 9 \times 10^7$ CM/SEC.
$S_\epsilon \times 10^{14}$ EV-CM^2/ATOM
4·0
3·2
2·4
1·6
·8
0
2
4
6
8
10
12
Z_1

FIG. 24.

APPENDIX A

REFERENCES

(B-48) Bohr, Neils. K. Danske Videnskab Selskab. Matt. Fys. Medd. 18 #8 (1948)

(D-60) Duckworth, H.E. Mass Spectroscopy. Cambridge University Press (1960)

(F-47) Fermi, E. and Teller, E. Phys. Rev. 72 399 (1947)

(F-58) Firsov, O.B. J.E.T.P. 7 308 (1958)

(H-59) Handbook of Chem. & Phys. 40th ed. 1959 Chemical Rubber Publishing Co.

(L-54) Lindhard, J. K. Danske Videnskab Selskab. Matt. Fys. Medd. 28 #8 (1954)

(L-61) Lindhard, J. and Scharff, M. Phys. Rev. 124 128 (1961)

(L-61a) Lindhard, Scharff and Thomsen. Private communication from Professor Lindhard, to be published in Matt. Fys. Medd. Dan. Vid. Selsk.

(P-53) Phillips, J. A. Phys. Rev. 90 532 (1953)

(P-62) Powers, D. and Whaling, W. Phys. Rev. 126 61 (1962)

(S-56) Seitz, F. and Koehler, J.S. Solid State Physics 2 305 (1956)

(S-61) Strivastava, G.N. and Scott, G.D. Brit. J. Appl. Phys. 12 255 (1961)

(T-62) Teplova, Nikolaev, Dmitriev and Fateeva. J.E.T.P. 15 31 (1962)

(V-62) Van Wijngaarden, A., and Duckworth, H.E. Can. J. Phys. 40 1749 (1962)

(W-49) Warshaw, S.D. Phys. Rev. 76 1759 (1949)

(W-58) Whaling, W. Handbuch der Physik XXXIV 193 (1958)

(E-55) Everhart, Stone and Carbone. Phys.Rev. 99 1287 (1955)

SYMBOLS

a - screening parameter

a_o - $(\hbar^2/m\varepsilon)$ Bohr radius for the hydrogen atom

b - distance of closest approach in the collision of two charged particles

e - 2.718

E - laboratory energy of the projectile

ΔE - most probable energy loss of projectiles after traversing a particular film

$\frac{dE}{dx}$ - differential stopping power

k - coefficient of energy dependence of stopping cross-sections

m_o - reduced mass

M_1, m_1 - mass of projectile

M_2, m_2 - mass of scattering centre

N - stopping atoms/cc

N - number of collisions a projectile suffers in passing through a film

$N(\theta)$ - $N(\theta)d\omega$ angular distribution of ions emerging from the film per unit solid angle

P - exponent in energy dependence of S

$P(r)$ - potential energy of two charged particles separated by a distance r

r - separation distance

ΔR - range difference

S_o - observed stopping cross-section

S_t - total stopping cross-section

S_ϵ - electronic stopping cross-section

S_ν - nuclear stopping cross-section

S_ν^* - nuclear stopping cross-section in the forward direction

Symbols - cont'd

ΔT_v - energy loss for an elastic collision

v - projectile velocity

v_o - $(\mathcal{E}/\hbar^2)$ velocity of the electron in the first Bohr orbit of hydrogen

Z_1 - atomic number of projectile

Z_2 - atomic number of stopping atom

α - azimuthal angle at base of cone

$\mathcal{E}$ - elementary charge

ξ_ϵ - coefficient in electronic stopping cross-section formula

$\sigma(\Theta)$ - $d\sigma(\Theta)$ - differential scattering cross-sections

σ_T - cross-section for a scattering event with deflection angle greater than Θ_{min}

Θ - relative deflection angle in a nuclear collision

Θ_{min} - smallest angular deflection considered in $\sigma(\Theta)$

θ - polar angle of projectile when leaving the film

ϕ - laboratory angle corresponding to a centre of mass angle Θ

$d\omega$ - unit solid angle

Ω_o - full width at half height of energy profile of transmitted ions

$\Omega_{R.P.}$ - contribution to Ω_o from the finite resolving power of the instrument

Ω_ϵ - contribution to Ω_o from the electronic straggling

Ω_F - contribution to Ω_o from the film non-uniformities